Dynamic loading of human engineered heart tissue enhances contractile function and drives a desmosome-linked disease phenotype

Bliley, J.M.; Vermeer, M.C.S.C.; Duffy, R.M.; Batalov, I.; Kramer, D.; Tashman, J.W.; ... ; Feinberg, A.W.

Citation

Bliley, J. M., Vermeer, M. C. S. C., Duffy, R. M., Batalov, I., Kramer, D., Tashman, J. W., … Feinberg, A. W. (2021). Dynamic loading of human engineered heart tissue enhances contractile function and drives a desmosome-linked disease phenotype. *Science Translational Medicine, 13*(603). doi:10.1126/scitranslmed.abd1817

CARDIOVASCULAR DISEASE

Dynamic loading of human engineered heart tissue enhances contractile function and drives a desmosome-linked disease phenotype

Jacqueline M. Bliley[1†], Mathilde C. S. C. Vermeer[2†], Rebecca M. Duffy[1], Ivan Batalov[1], Duco Kramer[3], Joshua W. Tashman[1], Daniel J. Shiwarski[1], Andrew Lee[1], Alexander S. Teplenin[4], Linda Volkers[4], Brian Coffin[5], Martijn F. Hoes[2], Anna Kalmykov[1], Rachelle N. Palchesko[1], Yan Sun[1], Jan D. H. Jongbloed[6], Nils Bomer[2], Rudolf A. de Boer[2], Albert J. H. Suurmeijer[7], Daniel A. Pijnappels[4], Maria C. Bolling[8], Peter van der Meer[2*], Adam W. Feinberg[1,5*]

The role that mechanical forces play in shaping the structure and function of the heart is critical to understanding heart formation and the etiology of disease but is challenging to study in patients. Engineered heart tissues (EHTs) incorporating human induced pluripotent stem cell (hiPSC)–derived cardiomyocytes have the potential to provide insight into these adaptive and maladaptive changes. However, most EHT systems cannot model both preload (stretch during chamber filling) and afterload (pressure the heart must work against to eject blood). Here, we have developed a new dynamic EHT (dyn-EHT) model that enables us to tune preload and have unconstrained contractile shortening of >10%. To do this, three-dimensional (3D) EHTs were integrated with an elastic polydimethylsiloxane strip providing mechanical preload and afterload in addition to enabling contractile force measurements based on strip bending. Our results demonstrated that dynamic loading improves the function of wild-type EHTs on the basis of the magnitude of the applied force, leading to improved alignment, conduction velocity, and contractility. For disease modeling, we used hiPSC-derived cardiomyocytes from a patient with arrhythmogenic cardiomyopathy due to mutations in the desmoplakin gene. We demonstrated that manifestation of this desmosome-linked disease state required dyn-EHT conditioning and that it could not be induced using 2D or standard 3D EHT approaches. Thus, a dynamic loading strategy is necessary to provoke the disease phenotype of diastolic lengthening, reduction of desmosome counts, and reduced contractility, which are related to primary end points of clinical disease, such as chamber thinning and reduced cardiac output.

INTRODUCTION

The heart is responsible for pumping blood throughout the body, and it must maintain sufficient cardiac output by adapting to differences in mechanical loads, including stretch during chamber filling (preload) and pressure that the heart must work against to eject blood (afterload). These physiological loads are critical to normal heart function; for example, during development, they contribute to heart muscle maturation resulting in increased cardiomyocyte alignment and hypertrophy (*1*). However, preload and afterload can also lead to maladaptive changes in heart muscle, as is the case in hypertension, myocardial infarction, and cardiomyopathies (*2*). In arrhythmogenic cardiomyopathy (ACM), mechanical loading of heart muscle that leads to adaptive hypertrophy in healthy individuals (such as during exercise) can accelerate ACM disease progression and lead to ventricular dilation and reduced contractility (*3*, *4*). Current guidelines therefore recommend avoidance of competitive sports in patients with ACM (*5*). Over half of the reported cases of ACM are due to mutations in desmosomal genes including desmoplakin (*DSP*), plakoglobin (*JUP*), plakophillin-2 (*PKP2*), desmoglein-2 (*DSG2*), and desmocollin-2 (*DSC2*) (*6*). In particular, desmoplakin links the desmosomal plaque to the intermediate filament network within the cell, and lack of desmoplakin is associated with the earliest and highest mortality rate in mice compared to the other desmosomal proteins (*7*). Patients with loss-of-function and dominant-negative mutations in *DSP* demonstrate a particularly severe phenotype, often with skin fragility in addition to heart disease (*8*, *9*). The interplay between patient-specific genetic background and mechanical force is likely critical to understanding a range of cardiac disease states, including ACM.

Studying the effects of mechanical loading on adaptive and maladaptive changes in heart structure and function is challenging in human patients, driving the need to develop new approaches. Animals have been used to model a wide range of human cardiovascular disease states, but there are inherent differences in physiology, gene expression, and pharmacokinetics that limit the ability to replicate complex pathology (*10*). In vitro two-dimensional (2D) culture of cardiomyocytes on microengineered surfaces has been used to study structure-function relationships and to create region-specific ventricular myocardium (*11*, *12*). Muscular thin films (MTFs), consisting of cells cultured on a flexible film, have enabled these 2D platforms to measure contractility (*13*, *14*), and, combined with patient-specific human induced pluripotent stem cell (hiPSC)–derived cardiomyocytes, can model cardiomyopathies such as Barth's syndrome

---

[1] Regenerative Biomaterials and Therapeutics Group, Department of Biomedical Engineering, Carnegie Mellon University, Pittsburgh, PA 15213, USA. [2] Department of Cardiology, University of Groningen, University Medical Center Groningen, 9713 GZ Groningen, Netherlands. [3] Department of Dermatology, University of Groningen, University Medical Center Groningen, 9713 GZ Groningen, Netherlands. [4] Department of Cardiology, Heart Lung Center Leiden, Leiden University Medical Center, 2333 ZA Leiden, Netherlands. [5] Department of Materials Science and Engineering, Carnegie Mellon University, Pittsburgh, PA 15213, USA. [6] Department of Genetics, University of Groningen, University Medical Center Groningen, 9713 GZ Groningen, Netherlands. [7] Department of Pathology, University of Groningen, University Medical Center Groningen, 9713 GZ Groningen, Netherlands. [8] Department of Dermatology, University of Groningen, University Medical Center Groningen, 9713 GZ Groningen, Netherlands.

*Corresponding author. Email: feinberg@andrew.cmu.edu (A.W.F.); p.van.der.meer@umcg.nl (P.v.d.M.)

†These authors contributed equally to this work.

(*15*). However, 2D cardiomyocytes are adhered to a surface (*16*) and thus do not have the same mechanical cell-cell coupling as found in the native heart (*17*). To address this, researchers have developed more physiologically relevant 3D engineered heart tissues (EHTs) in the form of papillary muscle–like linear bundles (*18*–*20*), myocardium-like sheets (*21*–*25*), and ventricle-like chambers (*26*, *27*). Incorporating hiPSC-derived cardiomyocytes, fibroblasts, and/or endothelial cells, these EHTs more closely resemble the structure of native myocardium. Furthermore, combined with electrical stimulation to drive contraction, these EHTs can also be functionally matured from an embryonic to a more mature phenotype (*28*). Although several groups have developed systems to modulate afterload on EHTs (*29*–*31*), most are still unable to model the adaptive or maladaptive changes in heart structure that occur in health and disease. Furthermore, many EHTs are limited by anchorage to static posts that result in isometric contraction (minimal contractile shortening) or incorporation into stretching systems that mimic physiologic strains but not physiologic loads (*32*, *33*).

Here, we report the development of a dynamic EHT (dyn-EHT) platform designed to mimic preload and afterload to model adaptive and maladaptive changes in heart structure and function. The goal is to better recapitulate the effect of hemodynamic loading on heart muscle to understand how forces alter gene expression, cytoskeletal organization, cell-cell coupling, electrophysiology, and force generation in control and diseased EHTs. Specifically, we sought to achieve (i) a dynamic preload and afterload that can drive adaptive changes in the EHT, (ii) physiologic contractile shortening of >10% (not isometrically constrained), and (iii) a straightforward optical readout of EHT contraction to facilitate experimental throughput. Our results reveal that embryonic stem cell (ESC)– and hiPSC-derived dyn-EHTs demonstrate adaptive remodeling under a physiologic loading regime, with structural and functional improvements. Furthermore, dyn-EHTs from patient-derived hiPSCs with desmoplakin mutations (DSPmut) that led to clinical ACM show maladaptive remodeling under the same loading range, with distinct structural abnormalities and functional deficits.

RESULTS

Development of the dyn-EHT platform for modeling preload and afterload

To create the mechanical loading platform, we fabricated EHTs around a polydimethylsiloxane (PDMS) strip used to both mechanically load the tissue and measure tissue contractile force. Briefly, human ESCs (hESCs) or hiPSCs were differentiated into cardiomyocytes, and primary adult cardiac fibroblasts were expanded (Fig. 1A). At day 0 of the experimental timeline, these cardiomyocytes and cardiac fibroblasts were mixed with collagen and Matrigel and then cast around elastic PDMS strips immobilized within PDMS wells. Fibroblasts within the mixture then compacted the extracellular matrix hydrogel into a linear EHT anchored to the PDMS strip. Cell and matrix compositions were optimized for the formation of a compact tissue with minimal collagen content and high contractility (fig. S1). All EHTs were maintained in the PDMS wells in a constrained state until day 14. From days 14 to 28, EHTs were either continually cultured in the constrained state (EHTs) or removed from the wells for dynamic culture (dyn-EHTs). In the constrained state (EHTs), the PDMS strip was immobilized within the well during the entire culture period. This is similar to most current EHT models, where the tissue is unable to appreciably shorten, and little active preload is provided to the tissue. In contrast, the dynamic state (dyn-EHTs) allowed for the tissue to beat in an unconstrained manner against the PDMS strip, which provided preload between heart muscle contractions and allowed for increased contractile shortening. Last, at day 28, both EHTs and dyn-EHTs were removed from culture and functionally assessed based on the ability of the tissue to contract and bend the PDMS strip.

Contractility assays were performed in an organ bath where one end of the PDMS strip was mounted in a block and the other end was free to move during each contraction (Fig. 1B). A custom MATLAB script was then used to analyze digital video to determine tissue length during contraction and therefore bending of the PDMS strip (https://doi.org/10.5281/zenodo.5034507) (Fig. 1C and movie S1). The force exerted by the tissue was based on known dimensions and elastic modulus of the PDMS strip. We selected strip thicknesses of ~130 μm (1×) or ~260 μm (8×), where the thicker strip was an about eightfold increase in load because bending stiffness is proportional to the inverse of the thickness cubed. Finite element modeling (FEM) demonstrated that the tensile force (diastolic force) applied to the tissue could be tuned from 0.05 to 5 mN on the basis of strip dimensions (fig. S2), with the 1× and 8× strips being selected for these studies with tensile forces from 0.05 to 0.9 mN (Fig. 1D and movie S2). To validate the FEM, a force transducer was used to measure the force required to bend the PDMS strip. Experimental strip bending forces displayed good agreement with the computational results (Fig. 1E and fig. S3).

8× dyn-EHT conditioning increases contractile stress generation

At day 28, the contractile function of EHTs cultured under constrained or dynamic conditions and 1× or 8× loading were assessed. There were differences in tissue length and contractility across all four conditions, with a clear improvement in force generation under dynamic 8× loading (Fig. 2A). The length of the EHT in the PDMS well during constrained culture was 6 mm, and all EHTs were analyzed out of the well. For the 1× loading, the constrained EHT maintained the same diastolic length as in the PDMS well, indicating that the force generated by the 1× strip did not stretch the EHT. For the 1× dyn-EHT, the diastolic tissue length actually decreased during culture from days 14 to 28, suggesting that the force generated by fibroblasts compacting the EHT was greater than the force exerted by the 1× strip. The 8× loading results were quite different, with the constrained EHT demonstrating a small increase in diastolic length when removed from the well. However, the 8× dyn-EHT showed the greatest change, with an ~50% increase in diastolic length. Measurements over time in culture indicated that tissue length stabilized in control 8× dyn-EHTs 1 week after removal from the PDMS well (fig. S4). The tissue contractile shortening showed a similar trend to the diastolic length, with the 8× EHT and 8× dyn-EHT having contractile shortening of 13 to 15% compared to only 5 to 8% for both 1× loading conditions (Fig. 2C). We found that 1× dyn-EHT had the least contractile shortening and, together with the observation of reduced tissue length, considered that tissue stiffness may have increased with 1× dyn-EHT culture. However, we did not find an increase in tissue elastic modulus in 1× dyn-EHTs (fig. S5). Thus, the reduced contractile shortening observed in 1× dyn-EHTs is likely due to a combination of disorganized sarcomeres (fig. S6, A to C) and reduced sarcomere length (fig. S6D).

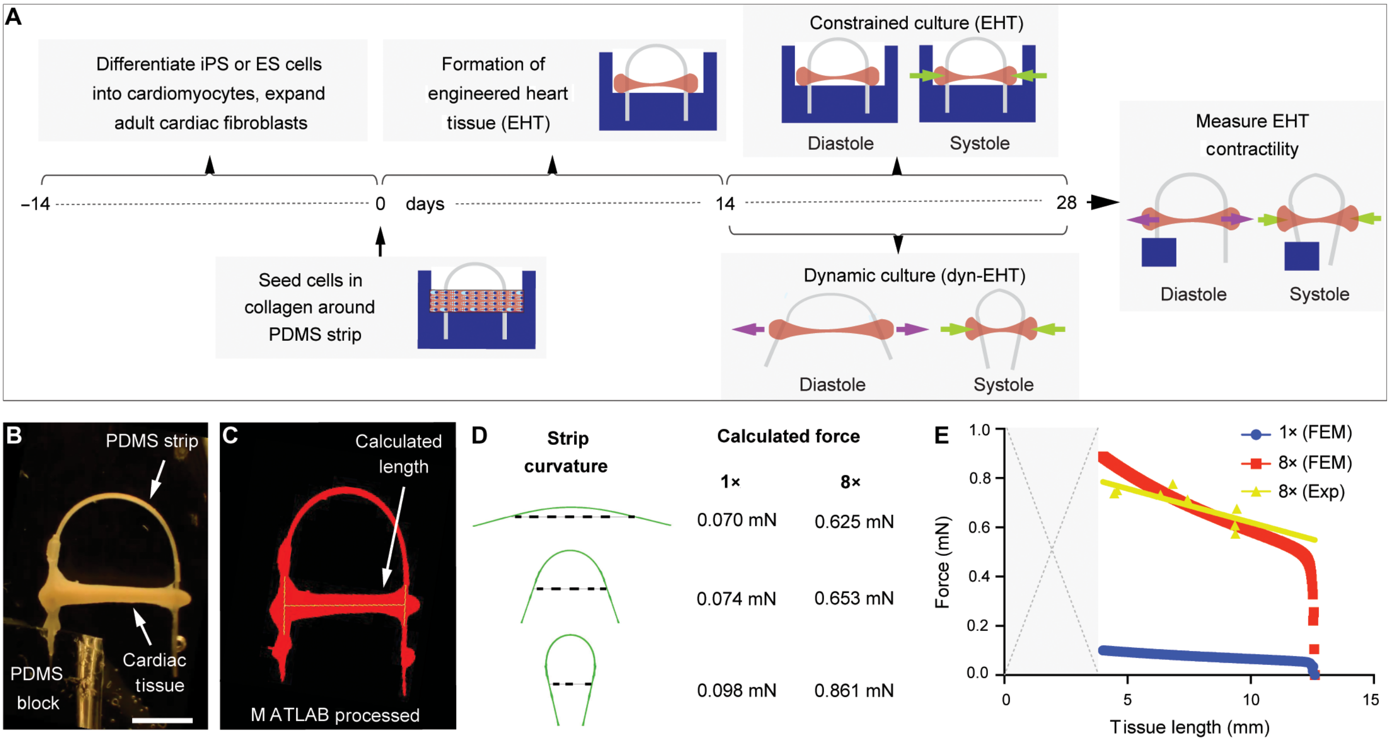

Fig. 1. EHTs can be fabricated around PDMS strips for loading and measuring tissue contractile force. (**A**) Schematic of EHTs cast around PDMS strips. First, cardiomyocytes are differentiated from either ESCs or hiPSCs, and cardiac fibroblasts are expanded. On day 0, cardiomyocytes and cardiac fibroblasts are cast within a collagen/Matrigel mixture around PDMS strips able to apply two different loads, either 1× or 8×. From days 0 to 14, cardiac fibroblasts compact the gel into a linear cardiac tissue between the ends of the PDMS strip. On day 14 and until day 28, tissues are exposed to constrained (EHTs) or dynamic (dyn-EHTs) loading. Arrows represent the relative amount of preload (pink) and afterload (green) on this tissue within either the constrained or dynamic condition. On day 28, all tissues are measured for contractile force based on the degree of PDMS strip bending. (**B**) Tissues were measured from the side to observe PDMS strip bending with contraction. Scale bar, 2.5 mm. (**C**) To determine the contractile tissue forces or load that is being applied during diastole, a custom-made MATLAB program was first used to track tissue change in length resulting in PDMS strip bending. (**D**) Finite element analysis was performed on both 1× and 8× strips to determine the tissue length (represented by the dashed line) needed to induce PDMS strip bending, which could subsequently be used to find the contractile tissue force, or the diastolic load being applied to the tissue. Representative tissue forces with 1×/8× PDMS strip curvature. Dashed line indicates length of the tissue. (**E**) Average force values obtained at each tissue length with either the 1× or 8× strips. Individual experimental data points (yellow triangles) are derived from force transducer measurements of strip bending at specific tissue lengths.

In terms of contractility, the stresses generated by the EHTs were greater for the 8× versus the 1× loading conditions with both spontaneous (Fig. 2D) and paced electrical stimulation (fig. S7, A to C). The 8× EHTs and 8× dyn-EHTs displayed elevated diastolic or tensile stresses (preload) compared to both 1× EHTs and 1× dyn-EHTs (Fig. 2E). The elevated diastolic stresses in the 8× group were also associated with higher contractile stresses (afterload). A graph of normalized stress for each condition showing one full contractile cycle demonstrates the relative difference in magnitude in the 1× groups compared to both 8× groups (Fig. 2F). The twitch stress (equivalent to the peak systolic stress minus the diastolic stress) observed in the 8× dyn-EHT was more than an order of magnitude greater than both 1× conditions and nearly four times greater than the 8× constrained EHT (Fig. 2G). Furthermore, the peak twitch stresses observed in the 8× groups were similar to other EHT systems (*29*, *34*, *35*). Despite increased twitch stresses, 8× dyn-EHTs did not display a positive force-frequency relationship or increased shortening at higher stimulation frequencies (fig. S8, A and B). Other researchers have also reported the absence of a positive force-frequency relationship in EHTs (*35*–*37*), despite signs of increased maturation. Related work suggests that a positive force-frequency relationship requires mature calcium handling (*38*), and it is likely that our 8× dyn-EHTs may need additional maturation through electrical stimulation (*28*, *39*) or treatment with insulin-like growth factor 1/neuregulin (*25*) to achieve this.

Differences in twitch kinetics were also observed under each loading condition. EHTs and dyn-EHTs displayed similar spontaneous beat frequencies under all loading conditions, which is unexpected considering the increased lengthening and diastolic stresses observed in 8× dyn-EHTs (fig. S9, A and B). Despite similar beat frequencies, 8× dyn-EHTs showed faster contraction times (fig. S9, C and D) and similar relaxation times (fig. S9E) compared to 1× dyn-EHTs. Combined with the increase contractile shortening, this led to an increase in the contractile and relaxation velocities in 8× dyn-EHTs compared to all other conditions (fig. S9, F and G). Similarly, contractile work and power increased in 8× dyn-EHTs compared to both 1× conditions (fig. S9, H and I), demonstrating a functional improvement in terms of producing more force over a longer distance in a shorter period of time. Similar results were obtained under 1-Hz electrical stimulation (fig. S10, A and B), with 8× dyn-EHTs displaying

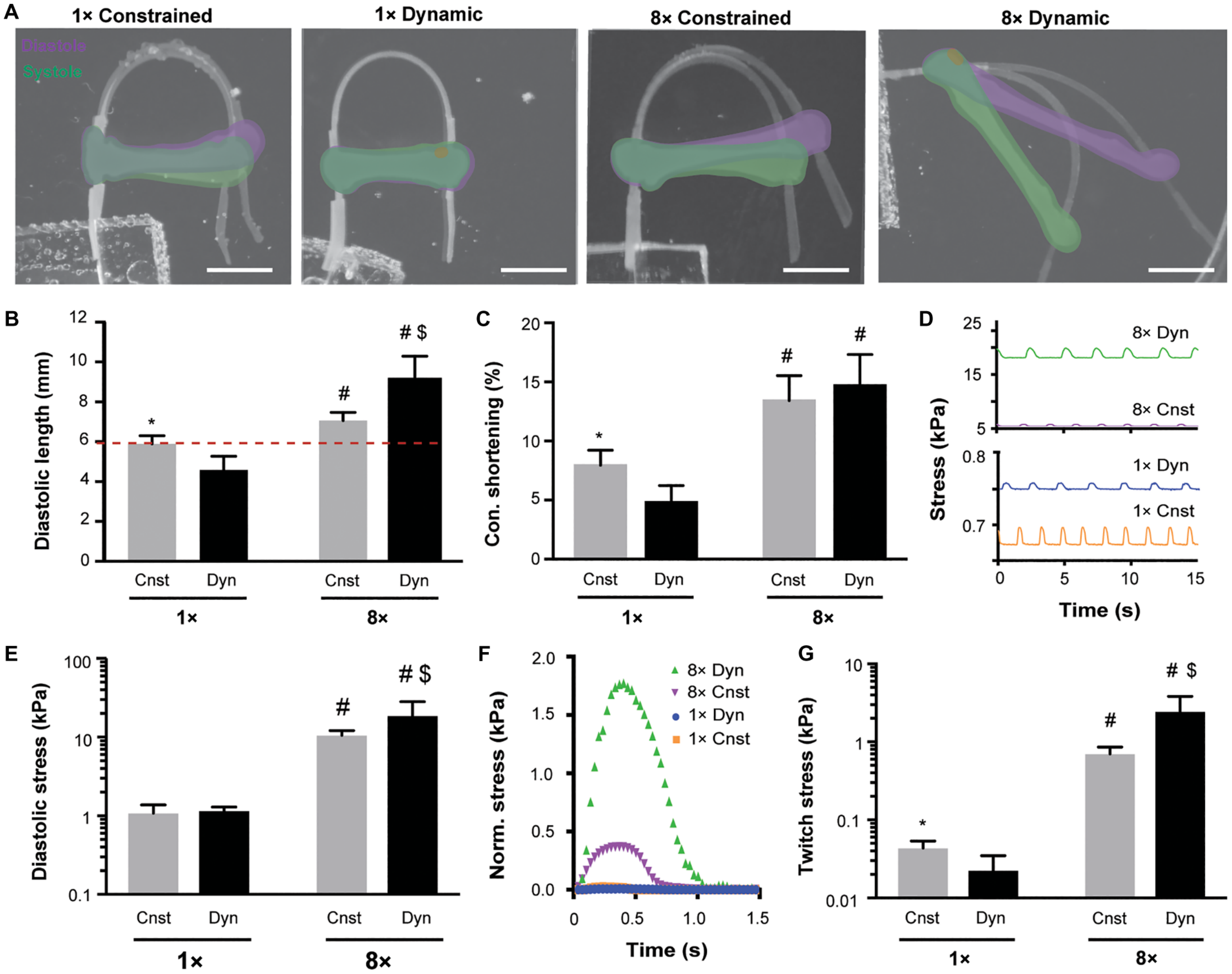

Fig. 2. PDMS strips can be used to mechanically load engineered heart muscle tissues. (**A**) Macroscopic tissue contractions overlaid with tissue in systole (green) and tissue in diastole (purple). Scale bars, 2.5 mm. (**B**) Diastolic tissue (resting) lengths. The red dashed line indicates the initial length of the tissue while it is immobilized within the PDMS well. (**C**) Contractile shortening under each loading type and condition. (**D**) Cardiomyocyte stress during contraction and relaxation at day 28. (**E**) Tissue diastolic stress/tensile stress. (**F**) Representative normalized cardiomyocyte twitch stresses for one single contraction. (**G**) Cardiomyocyte twitch stresses. All graphs show $n = 5$ per group for 8× EHT and 8× dyn-EHT, $n = 6$ per group for 1× dyn-EHT, and $n = 4$ per group for 1× EHT. Statistics based on two-way analysis of variance (ANOVA) with post hoc Holm-Sidak test. *$P < 0.05$ versus 1× dynamic; #$P < 0.05$ versus 1× dynamic and 1× constrained; \$$P < 0.05$ versus 8× constrained. One cardiomyocyte differentiation batch was used for all tissues in this figure. Cardiomyocyte cross-sectional area used for tissue stress measurements is displayed in fig. S23. All data represented as means ± SD.

increased contractile and relaxation velocities (fig. S10, C and D), work (fig. S10E), and power (fig. S10F) compared to all other conditions. These results highlight not only the unique impact that dynamic loading has on contractile stress for the 8× dyn-EHT but also that the magnitude of the load applied to the EHT (1× versus 8×) is important in driving these functional differences.

8× dyn-EHT improves maturation state based on myofibrillar alignment, gene expression, and electrophysiology

In terms of structure, the EHTs showed major differences in cytoskeletal organization as a function of the different loading conditions. This is relevant because the myocardium of the vertebrate heart already has highly aligned cardiomyocytes at early time points (*40*). Similarly, a number of studies using 2D and 3D engineered heart muscle tissue have shown that increases in cardiomyocyte alignment are associated with increases in contractile function (*11*, *23*, *24*, *41*). Fixing and staining the EHTs for the myofibrils confirmed that all tissues had a dense network of well-differentiated cardiomyocytes. However, it also revealed distinct differences in alignment between the 1× and 8× loading conditions (Fig. 3A). Quantification of the actin alignment confirmed that there were more myofibrils in the direction of the applied load in the 8× condition, showing the establishment of clear anisotropy. Comparison between the conditions using the orientational order parameter (OOP) further demonstrated

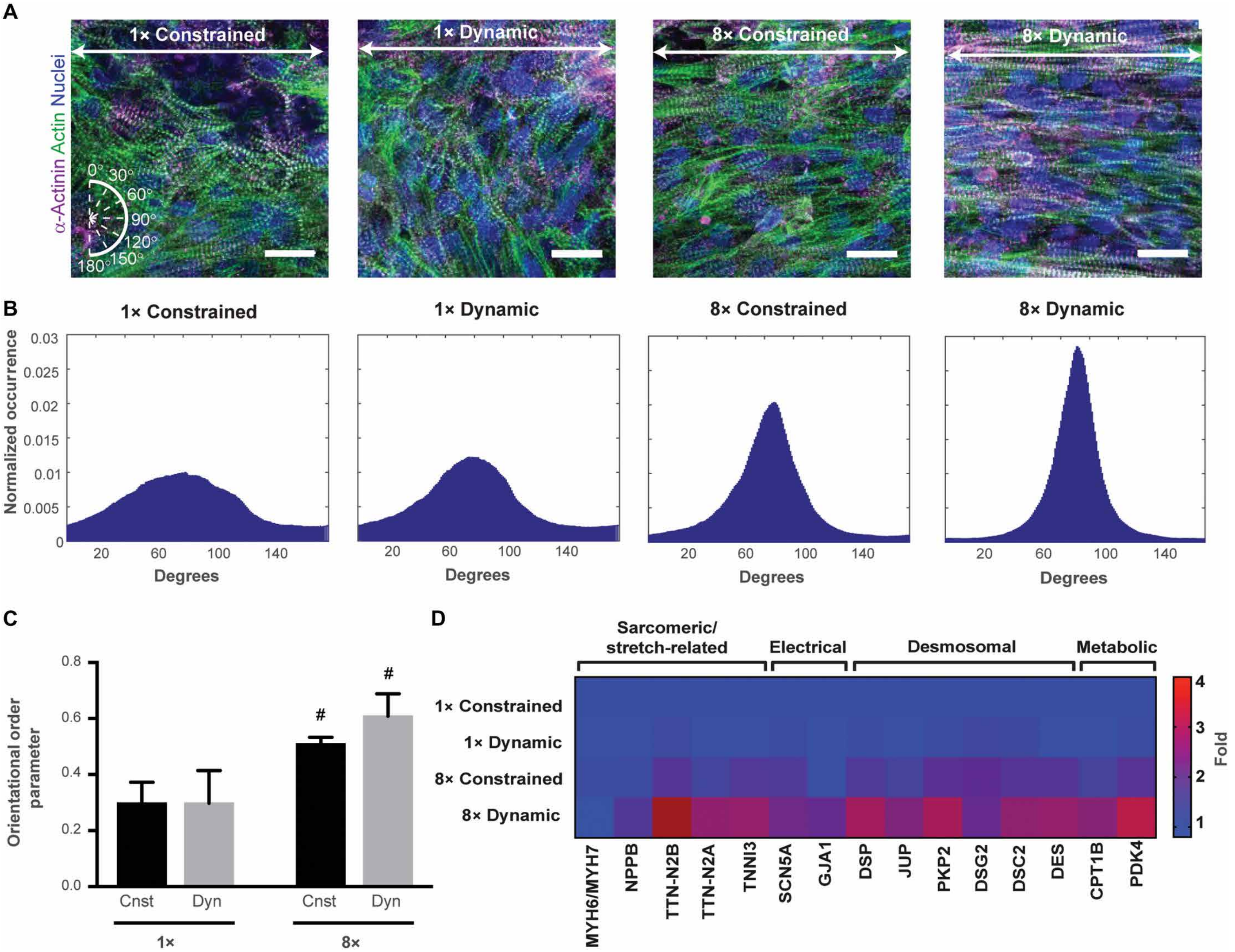

Fig. 3. Impact of loading on cardiomyocyte alignment and cardiac gene expression. (**A**) Microscopic images of tissue surfaces under each loading condition. The white arrow represents the tissue's longitudinal axis. Orientation angles were based on the white compass (bottom left) with a 90° orientation considered to be along the longitudinal axis of the tissue. Scale bars, 20 μm. (**B**) Histograms below each image display normalized actin angle occurrence of representative tissues from each loading condition. (**C**) Cardiomyocyte alignment (OOP) within engineered heart muscle tissues exposed to different loading conditions. $n = 3$ per group for 1× EHT, 1× dyn-EHT, and 8× EHT and $n = 4$ per group for 8× dyn-EHT. Statistics based on two-way ANOVA with post hoc Holm-Sidak test. #$P < 0.05$ versus 1× dynamic and 1× constrained. One cardiomyocyte differentiation batch was used to prepare all tissues in (A) to (C). (**D**) Heatmap showing log scale geometrical mean of gene expression relative to the 1× constrained loading condition. $n = 3$ tissues per group. One cardiomyocyte differentiation batch was used for gene expression analysis in (D). All data represented as means ± SD.

that alignment was significantly greater ($P < 0.05$) in the 8× versus 1× groups (Fig. 3B). Furthermore, both qualitative and quantitative analysis of myofibril alignment suggested that the 8× dyn-EHT condition had the greatest degree of anisotropy (Fig. 3, A to C). We also observed an increase in sarcomere length under the 8× dyn-EHT condition compared to both 1× conditions (fig. S6). This suggests that the 8× dyn-EHT condition produced sarcomeres that were more like those observed in adult human ventricular myocytes both in terms of alignment and spacing of ~2 μm (*42*).

Gene expression in the EHTs was also dependent on loading condition. Several genes typically associated with a more mature cardiomyocyte phenotype were up-regulated in the 8× dyn-EHT (Fig. 3D). We observed an up-regulation in sarcomere-related genes, including two different titin isoforms and troponin I. Expression of desmosomal genes—including *DSP*, *PKP2*, and *DSC2* and the intermediate filament gene *DES*—were also up-regulated in the 8× dyn-EHT condition. This is in line with previous results, showing that mechanical loading leads to increased expression of desmosomal genes (*43*) and further supports the idea that the 8× dyn-EHT may be better suited to study the functional and structural impacts of genetic mutations in desmosomal genes. Metabolic markers associated with fatty acid oxidation (the predominant form of metabolism in the adult heart), including *CPT1B* and *PDK4*, were also up-regulated within the 8× dyn-EHT. Furthermore, sodium channel *SCN5A* and gap junction Cx43 (*GJA1*) genes were also up-regulated in the 8× dyn-EHT group. Although not every gene examined showed an increase in the 8× dyn-EHT, it is evident that a number of genes associated with different aspects of the contractile apparatus in the cardiomyocytes were up-regulated.

The electrophysiology of the 8× dyn-EHT condition also showed important differences at both the cellular and tissue scales. Calcium imaging revealed uniaxial conduction along the length of the EHTs (Fig. 4, A to D). Quantification of the longitudinal conduction velocity based on the calcium wave propagation showed a statistically significant ($P < 0.05$) increase in the conduction velocity of 8× dyn-EHTs compared to the 1× conditions from about 5 to 10 cm/s (Fig. 4E). This is consistent with the changes in alignment and gene expression (Fig. 3), because increases in both cardiomyocyte aspect ratio and Cx43 gap junction expression are known to increase conduction velocity (*44*–*46*). At the cellular scale, sharp electrode measurements of cardiomyocyte resting membrane potential (RMP) were performed on the 1× and 8× dyn-EHTs. The RMP for adult ventricular cardiomyocytes is reported to be in the range of −70 to −90 mV depending on species and measurement technique (*47*, *48*). For hESC- and hiPSC-derived cardiomyocytes, the RMP is typically closer to zero and more fetal or embryonic like, though a number of studies have reported the ability to use engineered heart muscle tissue platforms to produce a more mature RMP (*28*, *47*, *49*). We observed that for the 1× dyn-EHT, there were two distinct populations, one with a less negative RMP (around −19 mV) and the other with a more negative RMP (around −62 mV) (Fig. 4F). However, for the 8× dyn-EHTs, the population of cardiomyocytes with an RMP around −20 mV was absent with an increase in the proportion of more negative cells with an RMP around −60 mV (Fig. 4G). This suggests that the increase in applied load between the 1× and 8× strips was able to drive immature cardiomyocytes toward a more mature phenotype in terms of RMP.

8× dyn-EHT reveals a disease phenotype based on a patient-derived model of ACM

A key advantage of engineered heart muscle tissue is the potential to study human disease states in an in vitro system using patient-specific hiPSC-derived cardiomyocytes. As a proof of concept, we chose to study ACM in a 50-year-old patient diagnosed with end-stage heart failure, who underwent a heart transplantation at the age of 45. The right ventricle of the explanted heart showed fat deposition and fibrosis, and the dilated left ventricle showed endocardial fibrosis (Fig. 5A). Immunofluorescent (IF) staining of the explanted heart revealed severe reduction of desmoplakin and other desmosomal proteins (Fig. 5B and fig. S11A). Next-generation sequencing with a targeted gene panel revealed two segregating mutations in *DSP*, where mutation c.273+5G>A was located on one *DSP* allele and mutation c.6687delA on the other *DSP* allele (fig. S11B) (*50*). Next, hiPSC-derived cardiomyocytes were generated from this patient (referred to as DSPmut) and a control wild-type line (fig. S12). Both mutated DSP protein transcripts were functionally evaluated in cultured cardiomyocytes. The *DSP*:c.273+5G>A splice site mutation did not result in alternative mRNA splicing, leading to a protein similarly sized as wild-type DSP. Nonetheless, protein transcripts from this allele were barely visible on Western blot. Mutation *DSP*:c.6687delA, located in the last exon, predicted a frameshift resulting in a premature stop codon p.(Arg2229Serfs*32). However, the truncated protein originating from this *DSP* allele was only detected after inhibition of nonsense-mediated mRNA decay p.(Arg2229Serfs*32), indicating

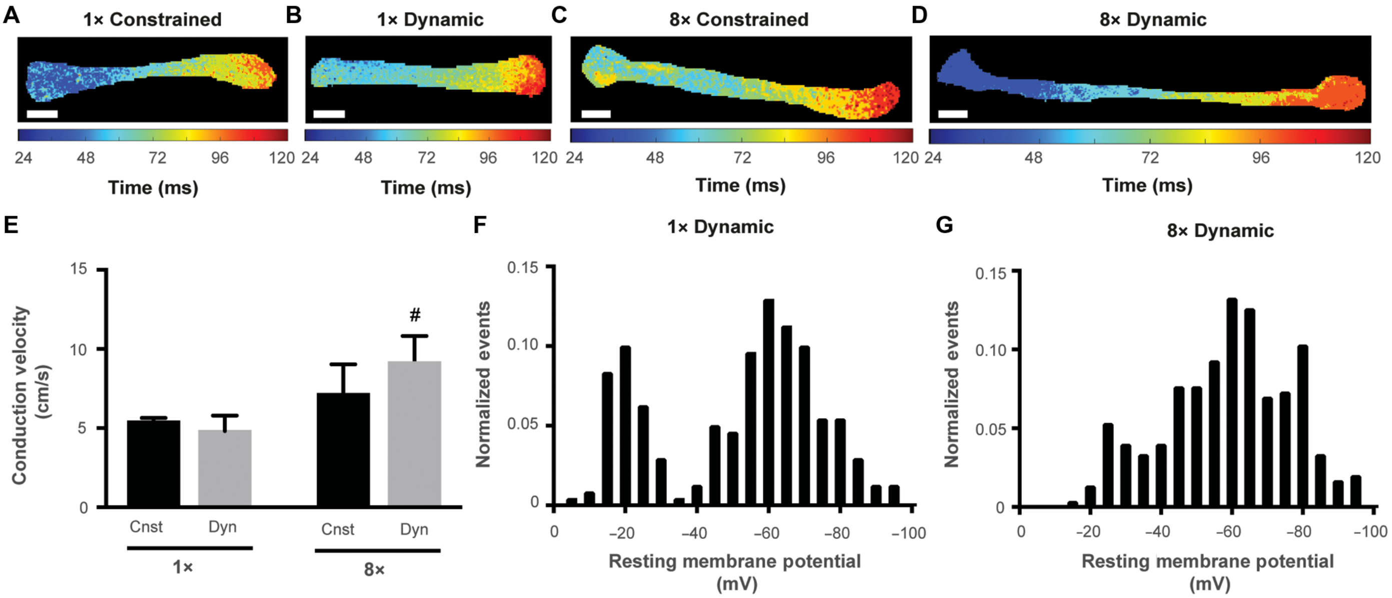

Fig. 4. 8× loading increases tissue conduction velocity and electrical excitability. (**A** to **D**) Calcium wave propagation in 1× constrained EHTs (A), 1× dyn-EHTs (B), 8× constrained EHTs (C), and 8× dyn-EHTs (D). Color map shows time delay of calcium wave as it travels across the tissue. (**E**) Conduction velocity obtained from calcium transients. $n = 4$ for 8× EHT, 8× dyn-EHT, and 1× dyn-EHT and $n = 3$ for 1× EHT. Statistics based on two-way ANOVA with post hoc Holm-Sidak test, where # indicates $P < 0.05$ compared to both 1× dynamic and 1× constrained loading conditions. One cardiomyocyte differentiation batch was used for conduction velocity measurements in (A) to (E). (**F** and **G**) Empirical probability distribution of cell RMPs obtained via sharp electrode measurements ($n = 3$ tissues per group, $n = 80$ cells measured throughout each tissue) within 1× dyn-EHT (F) and 8× dyn-EHT (G). One cardiomyocyte batch was used for sharp electrode measurements in (F) and (G). All data represented as means ± SD.

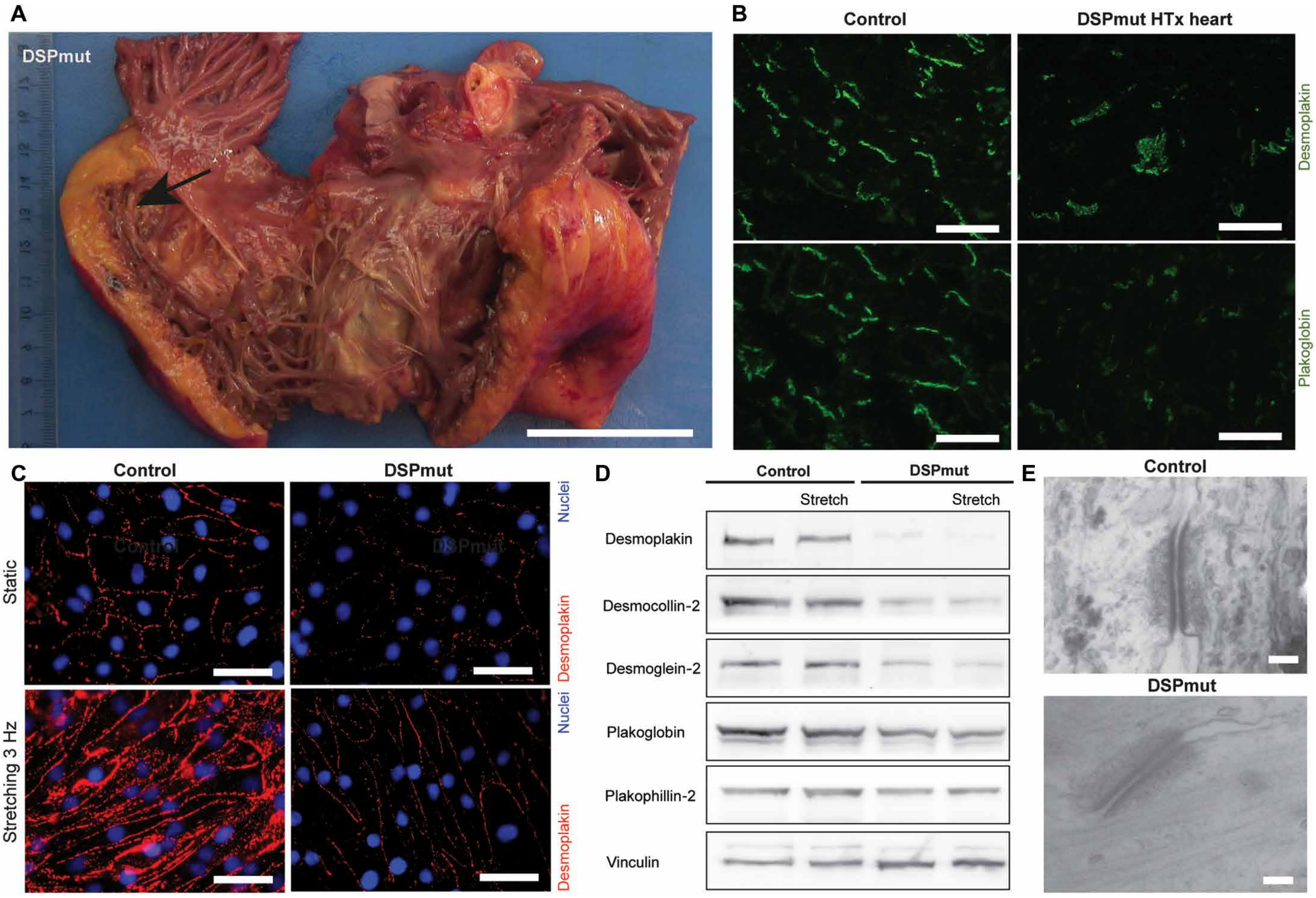

Fig. 5. In vitro phenotyping of DSPmut cardiomyocytes as a case study of ACM. (**A**) Explanted heart of the patient with DSPmut where the arrow points to fat deposition. Scale bar, 5 cm. (**B**) IF staining of desmoplakin and plakoglobin in explanted heart of patient with DSPmut in comparison to a control heart. Scale bars, 50 μm. (**C**) Desmoplakin localization in DSPmut compared to control cardiomyocytes upon application of 2D stretch. Data are representative for four cardiomyocyte differentiation batches. Scale bars, 50 μm. (**D**) Representative Western blot of desmosomal proteins in whole-cell lysates after mechanical stretching in 2D. Six DSPmut and four control cardiomyocyte differentiation batches were used for Western blot experiments. (**E**) TEM images of desmosomal ultrastructure. Scale bars, 50 nm.

that this protein is not normally expressed (fig. S13A). These hiPSC-derived cardiomyocytes displayed reduced desmoplakin IF signal compared to control (fig. S13B), and total desmoplakin protein abundance was threefold reduced in DSPmut cardiomyocytes compared to control (fig. S13, C and D). Among other cardiac desmosomal components, abundance of desmocollin-2 (DSC2) protein was twofold reduced (fig. S13C). The severe reduction in desmoplakin hence represents the pathology of a group of patients with loss-of-function mutations in *DSP*, leading to desmoplakin deficiency (*8*).

To understand the impact of 2D versus 3D culture, we first investigated 2D monolayers of DSPmut and control cardiomyocytes for membrane potential differences. DSPmut monolayers did not show any differences in maximum upstroke velocity nor action potential duration compared to controls (fig. S14, A to C). We then investigated desmosomal structure and localization before and after mechanical stretch using 2D Flexcell monolayer culture. Upon application of mechanical stretch, the controls repeatedly demonstrated a significant increase ($P < 0.05$) in localization of desmoplakin, plakoglobin, and plakophillin-2 to the cell periphery (Fig. 5C and fig. S15, A to C). However, no significant increase in localization to the cell periphery was observed in DSPmut monolayers exposed to 2D stretch (Fig. 5D and fig. S15, A to C). Despite these differences in desmosomal protein localization observed between DSPmut and control monolayers, whole-cell protein and mRNA abundances were not increased by mechanical stretch applied in a 2D setting (Fig. 5D and fig. S15D). This is in stark contrast to the up-regulation of desmosomal genes observed in control 8× dyn-EHTs (Fig. 3D). Although a minor increase in the interdesmosomal space was found, no changes in the number and protein density of desmosomes were observed after 2D stretch (Fig. 5E and fig. S15E).

Next, we used our 3D system to engineer constrained and dyn-EHTs using 1× and 8× loading. There were clear differences in DSPmut 8× dyn-EHTs compared to the other conditions, with a substantial increase in tissue diastolic length being observed (Fig. 6A and movie S3). For both DSPmut 1× and 8× dyn-EHTs, IF showed reduced desmoplakin expression compared to control (Fig. 6, B and C). Transmission electron microscopy (TEM) indicated less protein-dense desmosomes (Fig. 6, D and E, and fig. S16A) and reduced number of desmosomes in DSPmut 8× dyn-EHTs compared to control 8× dyn-EHTs (fig. S16B). These results established a clear impairment

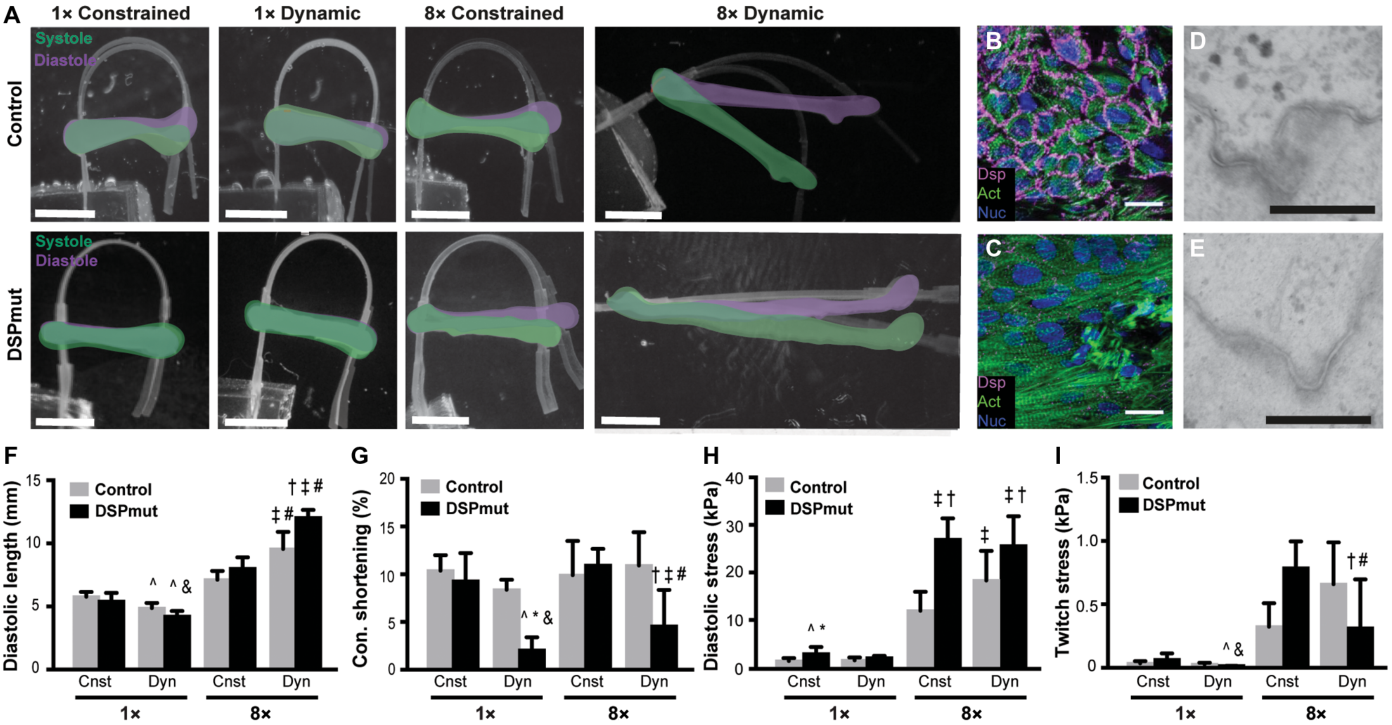

Fig. 6. The 8× dyn-EHT model progresses DSPmut tissues into disease. (**A**) Macroscopic tissue contraction of control and DSPmut tissues exposed to each loading amount (1× and 8×) and condition. Pictures are an overlay of tissues in systole (green) and diastole (purple). Scale bars, 2.5 mm. (**B** and **C**) Desmoplakin staining of control (B) and (C) DSPmut 8× dyn-EHTs. Scale bars, 20 μm. (**D** and **E**) TEM images of desmosomes in (D) control and (E) DSPmut 8× dyn-EHTs. Scale bars, 300 nm. (**F**) Diastolic tissue length in control and DSPmut tissues. (**G**) Contractile shortening in control and DSPmut tissues. (**H**) Diastolic stress in control and DSPmut tissues. (**I**) Cardiomyocyte twitch stress (kilopascal) in control and DSPmut tissues. Two-way ANOVA with a post hoc Holm-Sidak test was performed within each loading amount (either 1× or 8×). ‡ indicates $P < 0.05$ compared to control 8× constrained. † indicates $P < 0.05$ compared to control 8× dynamic. # indicates $P < 0.05$ compared to DSPmut 8× constrained. ^ indicates $P < 0.05$ compared to control 1× constrained. & indicates $P < 0.05$ compared to DSPmut 1× constrained. * indicates $P < 0.05$ control 1× dynamic. All graphs show $n = 8$ (DSPmut 1× constrained), $n = 6$ (DSPmut 1× dynamic), $n = 6$ (DSPmut 8× constrained), $n = 16$ (DSPmut 8× dynamic), $n = 8$ (control 1× constrained), $n = 6$ (control 1× dynamic), $n = 10$ (control 8× constrained), and $n = 10$ (control 8× dynamic). Ten CM differentiation batches were used for DSPmut tissues, and four batches were used for the control tissues. A larger number of DSPmut batches were included because of the high rate of breakage observed in DSPmut 8× dyn-EHTs. Cardiomyocyte cross-sectional area used for tissue stress measurements is displayed in fig. S24. All data represented as means ± SD.

in the desmosomal ultrastructure between control and DSPmut cardiomyocytes and were likely the reason why ~50% of the DSPmut 8× dyn-EHTs broke within 48 hours of removal from the PDMS well. The remaining intact DSPmut 8× dyn-EHTs lengthened out significantly ($P < 0.05$) more than control 8× dyn-EHTs (Fig. 6F). Contractile shortening was also significantly ($P < 0.05$) affected by loading conditions, where the DSPmut 1× and 8× dyn-EHTs showed a significant decrease from ~10 to <5% (Fig. 6G). Last, both DSPmut 8× EHTs and 8× dyn-EHTs showed elevated diastolic stresses compared to controls (Fig. 6H). However, there was a major difference in the twitch stress in DSPmut 8× EHTs and DSPmut 8× dyn-EHTs (Fig. 6I). DSPmut 8× EHTs showed a large increase in twitch stress compared to the control EHTs, suggesting that the increased diastolic stress may initially lead to elevated contractile stresses (afterload). In contrast, DSPmut 8× dyn-EHTs demonstrated a significant ($P < 0.05$) decrease in contractile force (fig. S17) and twitch stress compared to control EHTs, because the contractile shortening was also impaired.

Differences in contraction kinetics, work, and power were also observed between control and DSPmut tissues with respect to loading condition (figs. S18 and S19). For example, the DSPmut 8× EHTs and 8× dyn-EHTs had faster spontaneous beat rates and beat durations (fig. S18, A and B), suggesting that the increased diastolic stress from the 8× PDMS strips may be the cause. The DSPmut 8× dyn-EHTs also had faster contraction and relaxation times (fig. S18, C to E) compared to controls, though this was likely due to reduced contractile shortening because contraction and relaxation velocities were similar (fig. S18, F and G). The decreased contractile force and shortening for the DSPmut 8× dyn-EHTs resulted in decreased contractile work and power (fig. S18, H and I) compared to constrained and control tissues. Results were similar with 1-Hz electrical stimulation; but in this case, DSPmut 8× loaded tissues had faster contraction and relaxation times (fig. S19, A and B) but similar contractile and relaxation velocities (fig. S19, C and D) compared to controls. Also, similar between spontaneous and paced, DSPmut 8× dyn-EHTs had lower contractile work and power compared to controls (fig. S19, E and F). This further highlights the impaired function of DSPmut 8× dyn-EHTs and that the dynamic loading uniquely drives this disease-like phenotype. These results demonstrate that DSPmut 8× dyn-EHTs can manifest a disease-like phenotype in conditions of both dynamic culture and higher loading. This suggests that simulating both preload and afterload is required to model certain primary end points of cardiac disease in ACM.

DISCUSSION

The dyn-EHT platform builds on previous work from our laboratory and others that have used primary, hESC-, and hiPSC-derived cardiomyocytes to engineer cardiac tissues in vitro. It is critical to acknowledge the important contributions made by researchers using EHTs to model development and disease and implementing electromechanical conditioning to drive maturation (*18*–*22*, *28*, *29*, *31*, *32*, *49*, *51*–*53*). However, these 2D and 3D EHTs are generally isometrically constrained, which means that they undergo limited contractile shortening (1 to 5%) (*28*, *30*, *54*, *55*) and are exposed to minimal stretch with preload. For instance, current 3D EHTs are cast around PDMS, plastic posts, or frames that can bend during contraction but are otherwise rigid (*21*, *29*, *32*). Constraining EHTs therefore limits the ability to capture changes in tissue length that occur in disease states, such as dilation of the ventricles observed in certain cardiomyopathies (*56*).

Our results using the dyn-EHT platform demonstrate the importance of modeling aspects of both preload and afterload. We found that 8× dynamic culture of hESC- and hiPSC-derived dyn-EHTs enhanced contractility, resulting in increased tissue twitch stress, contractile shortening, and cardiomyocyte alignment. Furthermore, there was an increase in conduction velocity and the proportion of cells with a more negative RMP. Genes involved in action potential propagation were also up-regulated, including gap junctions and voltage-gated sodium channels. Other techniques known to mature engineered heart muscle tissue include electrical stimulation (*28*) and exposure to growth factors and hormones such as triiodothyronine (*57*), neuregulin (*25*, *58*), and glucocorticoids (*59*). By combining our mechanical loading platform with these approaches, we may be able to further enhance the function of our 8× dyn-EHTs.

Our results also demonstrate that dyn-EHT conditioning is important for revealing an ACM disease phenotype in patient-derived EHTs with mutations in desmoplakin. In 2D culture, DSPmut cardiomyocytes displayed similar desmosome number and protein density compared to controls despite a 65% reduction in desmoplakin and a 50% reduction in desmocollin-2. Investigating the consequence of these deficiencies in a 2D model of stretch (2D Flexcell monolayer culture), we only found a minor increase in the interdesmosomal space in DSPmut cardiomyocytes. This suggests that cardiomyocyte monolayers inadequately represent ACM progression because of being anchored to a 2D surface, which may contribute to increased stability to the desmosomes through support by other cell-matrix junctions. These 2D findings are in stark contrast to previous animal studies where desmosomal mutations result in loss of desmosomes between adjacent cardiomyocytes after endurance exercise (*4*). With 3D 8× constrained EHT culture, DSPmut tissues displaying elevated contractile stresses compared to control 8× constrained EHTs after removal from their constrained condition. This parallels what is observed in heart disease where studies have reported an increase in heart muscle contractility when initially exposed to pathological wall stresses (*60*, *61*). However, with extended 8× dyn-EHT culture, we observed deterioration of DSPmut function with tissue elongation and reduction in contractile stress, which resemble hallmarks of disease in human patients, including ventricular dilation and reduced ejection fraction. These data are supported by the decrease in desmosome amount and protein density observed in our ultrastructure findings. Together, these data suggest that current constrained cultures are limited in their ability to model diseases like ACM and researchers should consider the use of dynamic mechanical loading in their model in order to assess primary end points of disease.

Despite the current standardized ACM guidelines, it is still poorly understood how mechanical loading influences ACM disease progression. The patient investigated in this study suffered from end-stage heart failure requiring transplantation. Despite differing mutation predictions, the frameshift mutation actually resulted in full loss of protein product, whereas the splice mutation caused partial loss of protein product. Although observed in a single patient with ACM, the genetic background accumulated in severe desmoplakin deficiency is representative of a larger group of patients with loss of function–causing *DSP* variants (*62*, *63*), which give a severe cardiac phenotype often in combination with skin abnormalities (*8*). Future studies using the dyn-EHT system will require addressing *DSP* mutations that cause functionally altered desmoplakin protein products, in addition to other ACM causative genes.

Although the linear structure and uniaxial stresses in the dyn-EHT are a simplification of the lamellar architecture and biaxial stresses in the ventricular wall, it appears that we can capture aspects of stress-induced remodeling that have been challenging to observe in other EHT systems. In the case of the DSPmut EHT, the dynamic 8× loading resulted in considerable thinning and lengthening of the tissue. This suggests a possible corollary between our work and previous in vivo findings where tissue remodeling, including chamber thinning and eccentric dilation, is accelerated with elevated ventricular wall stresses (*64*, *65*). However, further studies would need to be performed to validate that the tissue remodeling observed in the 8× dyn-EHT is indeed comparable to ventricular dilation observed in vivo. Although there have been recent advances in engineering ventricle-like chambers (*27*, *66*–*68*), compared to our dyn-EHT, these chambers are much more difficult to fabricate, require a relatively large number of cells to form, and must be connected to a complicated flow system with valves and pressure transducers to generate preload.

The ability to mimic disease states using EHTs demonstrates the value of this technology for better understanding the link between genetics and function. Many studies have investigated heart diseases based on patient-specific mutations, using either genome-edited or patient-derived hiPSCs. For example, Hinson and colleagues (*29*) showed impaired contractility in EHTs with titin-truncating mutations, especially in response to an increased afterload. Wang *et al.* (*15*) showed reduced contractility in MTFs derived from patients with a genetic defect in Tafazzin. Healy and colleagues (*31*) used variable stiffness microfibers to modulate the afterload on genome-edited tissues lacking cardiac myosin binding protein C and found impaired contraction only when tissues were cultured on stiffer fibers. The dyn-EHT provides expanded capability by adding preload, which is of particular interest for modeling heart diseases that have a cardiomyocyte junctional or cytoskeletal component, which accounts for a large number of inherited genetic cardiomyopathies (*69*). This is further supported by our data showing that the distribution of mechanical load is different in a dynamic 3D environment when compared with either 2D or 3D constrained models. 8× dyn-EHTs formed using control hESC- and hiPSC-derived cardiomyocytes resulted in up-regulation of desmosomal genes, suggesting an elevated contribution of desmosomes in the adaptive response to mechanical load. Together, these findings suggest that 3D dynamic mechanical loading of EHTs may be better suited to investigate heart diseases with a cardiomyocyte junctional or cytoskeletal component.

As with any experimental system, there are limitations to consider in regard to the dyn-EHT platform. First, the dimensions of the PDMS strip determine the bending stiffness and the load applied to a tissue. Although it is straightforward to change the PDMS bending stiffness, this cannot be changed once integrated into the EHT. Second, although cardiomyocytes were derived from hESCs or hiPSCs, the cardiac fibroblasts were commercially available and derived from a healthy donor. This was done to minimize variability that can occur between hESC and hiPSC differentiations. Of particular importance is that a constant ratio of cardiac fibroblasts (10%) was used for every study; however, it is possible that use of higher or lower concentrations of cardiac fibroblasts may affect the remodeling observed in the dyn-EHT system. Last, we did not observe arrhythmias in our DSPmut 8× dyn-EHTs, which commonly occur during the course of ACM disease progression. There could be several reasons for this. First, the linear architecture of our tissues with highly aligned cells has essentially 1D conduction and limits our ability to detect arrhythmias (*70*). Second, arrhythmia in ACM occurs in the presence of abnormal collagen deposition and lipid droplets, and we did not observe either in our DSPmut tissues. This is expected given that these changes take years to manifest in patients and our tissues were cultured for only 1 month. Furthermore, only the cardiomyocytes were patient specific, whereas the cardiac fibroblasts were not. There is disagreement in the literature whether it is the cardiomyocytes alone or in combination with other cell types that drives arrhythmia (*71*–*73*). Many studies indicate that fibrosis, cardiomyocyte death, and fibro-fatty infiltration are the substrate for triggering arrhythmia (*74*). However, there is also evidence that arrhythmias in ACM can precede structural abnormalities (*75*). In total, our results provide some insight as the fact that we do not observe arrhythmia in DSPmut 8× dyn-EHTs suggests that more complex 3D tissue architecture, fibro-fatty infiltration, and additional cell types are contributing factors.

In conclusion, we have developed a model of mechanical loading of EHTs (dyn-EHTs) by incorporating a PDMS strip whose deformation can be used to determine tissue contractile forces but can also be used to mechanically load tissues. By incorporating a strip with sufficient load in a dynamic condition (8× dyn-EHTs), we were able to improve the function of control EHTs. Dynamic loading was also important in studying ACM disease progression in patient-derived EHTs with a desmoplakin mutation.

MATERIALS AND METHODS

Study design

The research objectives for this in vitro study were to (i) demonstrate that we can modulate the load on engineered heart muscle tissues and (ii) demonstrate improved function over current engineered heart muscle tissue models with minimal preload. We then (iii) validated that dynamic mechanical loading is important in creating in vitro disease models for studying cardiac diseases. Last, we compared our disease model to currently used 2D culture techniques. To accomplish this, we used contractility and calcium wave propagation analysis, FEM, immunohistochemistry, sharp electrode measurements, gene expression, Western blot, Sanger sequencing, and electron microscopy. In this study, established stem cell lines and patient- and control-derived stem cell lines were generated and subsequently validated. We used multiple lines and multiple differentiations to ensure that a true effect was observed. Tissues from each disease status (DSPmut versus control) were randomly assigned to loading condition. Sample sizes were determined on the basis of preliminary experiments and were different for each assay. A minimum of three independent biological replicates were used, and multiple experiments were performed to confirm the data. When possible, blinded analysis of experimental data was performed. Because our research was performed in two separate research laboratories, we compared all datasets for proper consistency. Tissues and 2D cell cultures were excluded if culture conditions differed from our preset timelines.

Human study approval

This study conforms to the Declaration of Helsinki. Approval of human participants was granted by the medical ethics committee of the University of Groningen (METC 2015.213). Written informed consent was received before inclusion of patients. Skin biopsies were taken for fibroblast culture.

ESC culture, cardiomyocyte differentiation, and metabolic purification

Before differentiation, ESCs were maintained in Essential 8 (E8) medium (A1517001, Thermo Fisher Scientific) on Geltrex (A1413202, Thermo Fisher Scientific)–coated six-well plates with daily medium changes and passaged at 80% confluence (about every 2 to 4 days). For passaging, cells were washed with 1× phosphate-buffered saline (PBS) and incubated with TrypLE (12604021, Thermo Fisher Scientific) for 5 min at 37°C. Cells were then resuspended in Dulbecco's modified Eagle's medium/nutrient mixture F-12 (11320033, Thermo Fisher Scientific), centrifuged at 200*g* for 5 min, and replated on Geltrex-coated plates in E8 with 2.5 μM Rho-associated kinase inhibitor, thiazovivin (S1459, Selleck Chemicals). Cardiomyocyte differentiation of human HUES9 ESCs was accomplished by addition of factors that mimic mesoderm induction and cardiac specification during embryogenesis (*76*). On day 0 of differentiation, cells were washed once with 1× PBS and incubated with RPMI/B27 media containing RPMI 1640 (21870076, Thermo Fisher Scientific) supplemented with 1% (v/v) L-glutamine (25030081, Thermo Fisher Scientific) and B27 supplement (17504044, Thermo Fisher Scientific) plus 6 μM CHIR99201 (C-6556, LC Laboratories) for 48 hours. On day 2, cells were washed with 1× PBS and medium was replaced with RPMI/B27 containing 2 μM Wnt C-59 (S7037, Selleck Chemicals) for another 48 hours. On day 6, medium was replaced with RPMI/B27. On days 8 and 10, medium was changed to chemically defined medium, 3 components (CDM3), consisting of RPMI 1640 supplemented with 1% (v/v) L-glutamine, L-ascorbic acid 2-phosphate sesquimagnesium salt hydrate >95% (213 μg/ml; A8960, Sigma-Aldrich), and human albumin (500 μg/ml; A9731, Sigma-Aldrich). On day 12, spontaneously beating cells were passaged for lactate-based metabolic selection of cardiomyocytes (*77*). To passage for purification, cells were incubated with TrypLE for 15 min at 37°C to enable single-cell dissociation. Cells were then reseeded in CDM3 with sodium lactate (CDM3L), consisting of RPMI 1640 without glucose (11879020, Thermo Fisher Scientific) supplemented with L-ascorbic acid 2-phosphate sesquimagnesium salt hydrate >95% (213 μg/ml; A8960, Sigma-Aldrich), human albumin (500 μg/ml; A9731, Sigma-Aldrich), and 7.1 mM sodium lactate (L4263, Sigma-Aldrich). Cells were maintained in CDM3L for several days before replacing back to CDM3 medium.

hiPSC culture, cardiomyocyte differentiation, and metabolic purification

Fibroblasts were cultured and reprogrammed to hiPSCs, using nucleofection with three plasmids—pCXLE-hSK, pCXLE-hMLN, and pCXLE-hOCT3/4—that were a gift from S. Yamanaka (Addgene plasmid nos. 27078, 27079, and 27076), according to previous reports (*78*, *79*). Pluripotent colonies were handpicked and dissociated to single cells using ACCUTASE (07920, STEMCELL Technologies) and TrypLE. hiPSCs were seeded on Geltrex (A1413202, Thermo Fisher Scientific)–coated plates in E8 medium with 5 μM ROCK inhibitor (Y27632, Bio-Connect). Differentiation was based on slight modifications of previously established protocols (*76*). Briefly, cells were incubated with RPMI 1640 (21870076, Thermo Fisher Scientific) supplemented with 5% knockout serum replacement (KOSR; 10828028, Gibco) containing factors CHIR99201 (13122, Cayman) and activin A (120-14E, PeproTech) for 48 hours. On day 2 of differentiation, cells were incubated with medium containing factors Wnt-C59 (5148/10, R&D Systems) and bone morphogenetic protein 4 (SRP3016, Sigma-Aldrich) for 48 hours. Cells were then maintained in previously reported CDM3 medium (*80*) until day 17. Day 17 after differentiation, cardiomyocytes were treated with dispase (07923, STEMCELL Technologies) and TrypLE to obtain a single-cell suspension. Cells were then reseeded for metabolic purification in CDM3L media with 2% KOSR. Cells were maintained in CDM3L for several days before replacing back to CDM3 medium. Cardiomyocytes were then used for 2D and 3D experiments. To investigate the effect of *DSP* mutation c.6687delA on protein expression, nonsense-mediated decay inhibition was performed on cardiomyocytes using a nonsense-mediated mRNA-decay inhibitor, 50 μM NMDi14 [previously mentioned (*81*), SML1538-5MG, Sigma-Aldrich] for 6 hours.

Cyclic stretch of 2D monolayers

Cardiomyocytes were replated as monolayers with identical cell density on BioFlex plates. Monolayers were subjected to cyclic stretch regimens using the Flexcell system FX-4000. To mimic daily intervals of endurance exercise, 22 hours of 15% stretch at 1 Hz was used, followed by 2 hours of 15% stretch at 3 Hz, for a total duration of 4 days.

Human cardiac ventricular fibroblast culture

Normal human ventricular cardiac fibroblasts were obtained from Lonza and expanded maximally to ensure use of a single-cell source throughout our experiments. Fibroblasts were used between passages 5 and 10 for all studies described in this paper. Cells were maintained in fibroblast growth medium–3 (CC-4526, Lonza) and passaged at 80% confluence.

Fabricating engineered heart muscle tissues around PDMS strips

To fabricate engineered heart muscle tissues around strips, first, PDMS wells were created. To create the wells, molds were designed in SolidWorks (fig. S20) and printed using either VeroWhitePlus RGD835 using an Objet Connex350 (Stratasys) or Dental SG resin (RS-F2-DGOR-01, Formlabs) on a Form 2 stereolithography printer. PDMS wells were created to cast the tissue around the strip by casting SYLGARD 184 PDMS (Dow Corning) in a 10:1 base–to–curing agent ratio. SYLGARD 184 was mixed before casting using a THINKY conditioning mixer (Phoenix Systems) for 2 min at 2000 rpm each for mixing and defoaming. Molds were degassed for 30 min under vacuum to remove bubbles and cured at 65°C for 4 hours, and then PDMS wells were removed from the molds. Subsequently, PDMS strips were laser-cut from PDMS sheets (BioPlexus Inc.), either ~130 μm (SH-20001-005) or ~260 μm (CUST-20001-010) thick, using a ProtoLaser U3 (LPK5). Because bending resistance of the strip is proportional to the inverse of thickness-cubed, a profilometer was used to determine each strip thickness (VHX-5000).

Before engineered heart muscle tissue fabrication, wells were sterilized via sonication in 50% (v/v) ethanol for 30 min, and PDMS strips were sterilized with ultraviolet-ozone treatment for 15 min. Sterile PDMS wells were fixed to one well of a six-well culture plate using a thin layer of vacuum grease. PDMS wells were then incubated with 1% (w/v) Pluronic F-127 (P2443, Sigma-Aldrich) for 10 min to reduce collagen attachment to the well and washed three times in 1× PBS. Sterile PDMS strips were then placed in the slits in the bottom of the well to secure the strip during heart muscle tissue casting. Collagen I derived from rat tail (354249, Corning) and Matrigel (354263, Corning) were used to fabricate engineered heart muscle tissues around the PDMS strips. The final concentrations were collagen I (1 mg/ml), Matrigel (1.7 mg/ml), 10% 10× PBS, 2.3% 1 N NaOH, and 18.75×10^6 total cells/ml consisting of 90% cardiomyocytes and 10% cardiac fibroblasts. Ingredients were mixed with a pipette, and then 80 μl of the cell mixture was pipetted into each well around the PDMS strip. Six-well plates containing the molds and cell suspension were then placed at 37°C to allow for gelation. After a 45-min incubation period, engineered heart muscle tissues were incubated and maintained in heart muscle tissue media containing RPMI 1640 supplemented with 1% (v/v) KOSR.

Engineered heart muscle tissue loading

To mechanically load the tissues, strips of either ~130- or ~260-μm thickness were incorporated into the engineered heart muscle tissues during tissue formation, where the thicker strip represented an approximate 8× increase in load being applied to the tissue. On day 14, tissues were exposed to either constrained or dynamic mechanical loading from days 14 to 28. Under the constrained condition, the strip was held immobilized within the well throughout the entire culture period, whereas the dynamic condition allowed for the tissue to beat in an unconstrained manner against the PDMS strip. For dynamic loading, a PDMS block with a vertical cut was adhered to a new well with vacuum grease, and one end of the strip was fixed into the vertical cut in the PDMS block. Tissues were maintained in heart muscle tissue media in either constrained or dynamic culture until day 28.

Calcium imaging and conduction velocity measurements

To assess tissue conduction velocity, engineered heart muscle tissues were stained with a calcium indicator dye, 1 μM Fluo-4 (F14201, Thermo Fisher Scientific). An excitation-contraction decoupler, 10 μM blebbistatin (B0560, Sigma-Aldrich) was used to prevent tissue contraction, which would make it difficult to perform automated analysis on the calcium wave front. Calcium imaging (50 frames per second) was performed using a Prime 95B scientific complementary metal-oxide semiconductor camera (Photometrics) mounted on an epifluorescent stereomicroscope (Nikon SMZ1000) with a green fluorescent protein filter and an X-Cite lamp (Excelitas). Conduction velocity (centimeter per second) was calculated by obtaining the average distance of the tissue in centimeters and dividing that by the average time (in seconds) that it takes for the wave to traverse the tissue. For activation maps, calcium transients from spontaneous contractions were then postprocessed with a custom-made MATLAB program using calcium signal peak times and cross-correlation (https://doi.org/10.5281/zenodo.5034507).

Tissue contractility assay and measurements

During engineered heart muscle tissue contraction, the tissue decreases in length, resulting in PDMS strip bending. Based on known dimensions and elastic modulus of the PDMS strip, the degree of strip bending can be used to determine the force the tissue is exerting during contraction. Twitch stress measurements were found by dividing average twitch force by average cross-sectional area of cardiomyocytes within the tissue (figs. S23 and S24). To image PDMS strip bending due to engineered heart muscle tissue contraction, a PDMS block with a vertical cut was adhered to a petri dish using vacuum grease and one end of the strip was fixed into the vertical cut in the PDMS block. During the contractility assay, tissues were maintained in Tyrode's solution (T2145, Sigma-Aldrich) on a custom-heated stage at 37° ± 1°C. The PDMS strip was imaged with a Nikon DSLR camera mounted on a Nikon SMZ1500 stereomicroscope to visualize strip bending due to engineered heart muscle tissue contraction. A custom-made MATLAB program was created to automatically calculate the change in length of the tissue from contraction videos (fig. S21). Look-up tables relating tissue length to force required to induce PDMS strip bending were created using a FEM. Look-up tables were derived from FEM of strip bending performed in ANSYS software (fig. S22). Modeling was performed by applying known displacements to the PDMS strip and then obtaining the reaction force associated with these displacements. The PDMS strip was modeled as a 3D deformable, extruded solid with two different thicknesses. The strip was considered linearly elastic, isotropic, and incompressible with a Young's modulus of 1.59 MPa for ~130-μm strips and 1.89 MPa for ~260-μm strips, respectively. Elastic moduli were derived from tensile testing of laser-cut dog bones derived from each respective material. Briefly, dog bones were mounted on an Instron 5943 and stretched at a rate of 1 mm/min. The average cross-sectional area of the dog bones was manually determined before testing, and dog bone thickness was determined with profilometer (VHX-1000) measurements. Stress was calculated by dividing the force by the cross-sectional area of the strip. Stress was then plotted against the strain, and slopes of the individual curves in the linear region of the stress-strain graph (0 to 10%) were averaged to obtain the elastic modulus of the PDMS.

Sharp electrode measurements

Tissues were washed five times with Tyrode's solution. Glass microelectrodes with tip resistances of 8 to 20 megohm when filled with 3 M potassium chloride (KCl) were used to impale the tissues. Measurements were performed using a MultiClamp 700B amplifier, and analog signals were low-pass–filtered (10 kHz) and digitized at a sample rate of 20 kHz via a Digidata 1440A A/D digitizer (both Axon Instruments/Molecular Devices). All recordings were performed at room temperature. Data were analyzed using pCLAMP 10.7 acquisition software (Axon Instruments), Excel (version 2010, Microsoft), and Prism 7.02 (GraphPad Software). Both datasets were normalized by dividing the number of events in each bin by the total number of events. Only measurements with stable RMPs were included in this study.

Gel electrophoresis and Western blotting

Cellular proteins from cells or tissues were extracted using a buffer containing 62 mM tris-hydrochloride, 2.5% SDS, and 1 mM EDTA. Before extraction, protease inhibitor (11873580001, Roche), phosphatase inhibitor cocktail 3 (p2850, Sigma-Aldrich), and sodium orthovanadate were added. After protein quantification (Pierce), sample buffer was added (final solution contains 10% glycerol, 5% β-mercaptoethanol, and bromophenol blue). Samples were heated to 99°C before loading. Proteins were separated using SDS–polyacrylamide gel electrophoresis and transferred to polyvinylidene difluoride membranes using semidry or tank blotting. Membranes were blocked using 5% milk and incubated on a shaker overnight at 4°C with primary antibodies (table S1) and for 1 hour on a shaker at room temperature with secondary horseradish peroxidase–labeled antibodies. As loading control, either glyceraldehyde-3-phosphate dehydrogenase or vinculin was used depending on the protein's molecular weight. For detection, electrochemiluminescence was used. Protein quantification was done with the ImageJ gel analyzer.

Immunofluorescence

For whole-mount imaging, engineered heart muscle tissues were fixed in 4% formaldehyde (15710, Electron Microscope Sciences) overnight and permeabilized with Triton X-100 (9002-93-1, Sigma-Aldrich) for 1 hour at room temperature. Two-dimensional cultured cells were fixed and permeabilized with ice-cold methanol:acetone for 10 min. Ex vivo tissues were cut with a cryostat and air-dried before staining. Tissues/cells were incubated with bovine serum albumin/PBS blocking buffer containing serum of secondary antibodies' host. Tissues/cells were then incubated with primary antibodies in blocking buffer accordingly. After primary antibody incubation, tissues were washed with 1× PBS. Alexa Fluor 488– or Alexa Fluor 555–labeled antibodies were used as secondary antibodies in blocking buffer, and tissues/cells were incubated accordingly with either Hoechst or 4′,6-diamidino-2-phenylindole for nucleus labeling. Tissues/cells were then washed with 1× PBS and mounted for imaging. Primary antibodies are listed in table S1.

Engineered heart muscle tissue imaging and actin alignment analysis

Confocal images were acquired with a Zeiss LSM 700 laser scanning microscope with a 63× (numerical aperture 1.4) oil immersion objective to obtain *z*-stacks of the tissue surface. Maximum intensity projections of *z*-stacks ($n = 10$ per tissue, about 20-μm depth) were used for cardiomyocyte alignment quantification (actin alignment quantification). A custom MATLAB code was used to quantify the angular distribution of actin filaments on the basis of previous described methods (https://doi.org/10.5281/zenodo.5034507) (*82*). Briefly, a threshold was applied on the basis of actin filament prominence and used to determine which orientations to take into account for the analysis. The α-actinin channel was then used to create a binary mask for cardiomyocyte locations, which was used to determine cardiomyocyte alignment. Using combinations of these masks, we were able to determine the alignment of cardiomyocytes versus fibroblasts within the tissues. Angular distribution of actin filaments were then used to calculate the OOP—a measure of alignment, where OOP values close to 1 indicate completely coaligned actin filaments and values close to 0 indicate an isotropic distribution of actin filaments. An average OOP was obtained for each sample by considering angular distributions of actin filaments within all *z*-stacks ($n = 10$ per tissue).

Statistical analysis

Data are represented as means ± SD. Statistical analysis was performed using Prism software (GraphPad) or SigmaPlot. Datasets were assessed for normality using a Shapiro-Wilk normality test. Homogeneity of variances was assessed with either Brown-Forsythe or Levene median test. Outliers were defined with robust regression with outlier detection (ROUT, $Q = 1$) testing. Statistical significance was considered a P value < 0.05, and appropriate statistical tests were chosen on the basis of experimental conditions and data. If data did not meet assumptions of normality and homogeneity of variances, then either the data were transformed (to meet these assumptions) or an appropriate nonparametric test was used.

SUPPLEMENTARY MATERIALS

stm.sciencemag.org/cgi/content/full/13/603/eabd1817/DC1
Materials and methods
Figs. S1 to S24
Tables S1 and S2
Movies S1 to S4
Data file S1

View/request a protocol for this paper from *Bio-protocol*.

REFERENCES AND NOTES

1. S. E. Lindsey, J. T. Butcher, H. C. Yalcin, Mechanical regulation of cardiac development. *Front. Physiol.* **5**, 318 (2014).
2. A. M. Katz, Maladaptive growth in the failing heart: The cardiomyopathy of overload. *Cardiovasc. Drugs Ther.* **16**, 245–249 (2002).
3. F. M. Cruz, D. Sanz-Rosa, M. Roche-Molina, J. García-Prieto, J. M. García-Ruiz, G. Pizarro, L. J. Jiménez-Borreguero, M. Torres, A. Bernad, J. Ruíz-Cabello, V. Fuster, B. Ibáñez, J. A. Bernal, Exercise triggers ARVC phenotype in mice expressing a disease-causing mutated version of human plakophilin-2. *J. Am. Coll. Cardiol.* **65**, 1438–1450 (2015).
4. R. Martherus, R. Jain, K. Takagi, U. Mendsaikhan, S. Turdi, H. Osinska, J. F. James, K. Kramer, E. Purevjav, J. A. Towbin, Accelerated cardiac remodeling in desmoplakin transgenic mice in response to endurance exercise is associated with perturbed Wnt/β-catenin signaling. *Am. J. Physiol. Heart Circ. Physiol.* **310**, H174–H187 (2016).
5. S. M. Al-Khatib, W. G. Stevenson, M. J. Ackerman, W. J. Bryant, D. J. Callans, A. B. Curtis, B. J. Deal, T. Dickfeld, M. E. Field, G. C. Fonarow, A. M. Gillis, C. B. Granger, S. C. Hammill, M. A. Hlatky, J. A. Joglar, G. N. Kay, D. D. Matlock, R. J. Myerburg, R. L. Page, 2017 AHA/ACC/HRS Guideline for management of patients with ventricular arrhythmias and the prevention of sudden cardiac death. *Circulation* 10.1161/CIR.0000000000000549 (2018).
6. A. D. den Haan, B. Y. Tan, M. N. Zikusoka, L. I. Lladó, R. Jain, A. Daly, C. Tichnell, C. James, N. Amat-Alarcon, T. Abraham, S. D. Russell, D. A. Bluemke, H. Calkins, D. Dalal, D. P. Judge, Comprehensive desmosome mutation analysis in North Americans with arrhythmogenic right ventricular dysplasia/cardiomyopathy. *Circ. Cardiovasc. Genet.* **2**, 428–435 (2009).
7. G. Ian Gallicano, P. Kouklis, C. Bauer, M. Yin, V. Vasioukhin, L. Degenstein, E. Fuchs, Desmoplakin is required early in development for assembly of desmosomes and cytoskeletal linkage. *J. Cell Biol.* **143**, 2009–2022 (1998).
8. T. Maruthappu, A. Posafalvi, S. Castelletti, P. J. Delaney, P. Syrris, E. A. O'Toole, K. J. Green, P. M. Elliott, P. D. Lambiase, A. Tinker, W. J. McKenna, D. P. Kelsell, Loss-of-function desmoplakin I and II mutations underlie dominant arrhythmogenic cardiomyopathy with a hair and skin phenotype. *Br. J. Dermatol.* **180**, 1114–1122 (2019).
9. M. Pigors, A. Schwieger-Briel, R. Cosgarea, A. Diaconeasa, L. Bruckner-Tuderman, T. Fleck, C. Has, Desmoplakin mutations with palmoplantar keratoderma, woolly hair and cardiomyopathy. *Acta Derm. Venereol.* **95**, 337–340 (2015).
10. J. Egido, C. Zaragoza, C. Gomez-Guerrero, J. L. Martin-Ventura, L. Blanco-Colio, B. Lavin, B. Mallavia, C. Tarin, S. Mas, A. Ortiz, J. Egido, Animal models of cardiovascular diseases. *J. Biomed. Biotechnol.* **2011**, 497841 (2011).
11. A. W. Feinberg, P. W. Alford, H. Jin, C. M. Ripplinger, A. A. Werdich, S. P. Sheehy, A. Grosberg, K. K. Parker, Controlling the contractile strength of engineered cardiac muscle by hierarchal tissue architecture. *Biomaterials* **33**, 5732–5741 (2012).
12. I. J. Dornian, M. Chiravuri, P. van der Meer, A. W. Feinberg, X. Shi, Y. Shao, S. M. Wu, K. K. Parker, K. R. Chien, Generation of functional ventricular heart muscle from mouse ventricular progenitor cells. *Science* **326**, 429–249 (2009).
13. A. W. Feinberg, A. Feigel, S. S. Shevkoplyas, S. Sheehy, G. M. Whitesides, K. K. Parker, Muscular thin films for building actuators and powering devices. *Science* **317**, 1366–1370 (2007).
14. A. W. Feinberg, C. M. Ripplinger, P. Van Der Meer, S. P. Sheehy, I. Domian, K. R. Chien, K. K. Parker, Functional differences in engineered myocardium from embryonic stem cell-derived versus neonatal cardiomyocytes. *Stem Cell Rep.* **1**, 387–396 (2013).
15. G. Wang, M. L. McCain, L. Yang, A. He, F. S. Pasqualini, A. Agarwal, H. Yuan, D. Jiang, D. Zhang, L. Zangi, J. Geva, A. E. Roberts, Q. Ma, J. Ding, J. Chen, D. Z. Wang, K. Li, J. Wang, R. J. A. Wanders, W. Kulik, F. M. Vaz, M. A. Laflamme, C. E. Murry, K. R. Chien, R. I. Kelley, G. M. Church, K. K. Parker, W. T. Pu, Modeling the mitochondrial cardiomyopathy of Barth syndrome with induced pluripotent stem cell and heart-on-chip technologies. *Nat. Med.* **20**, 616–623 (2014).
16. C. P. Soares, V. Midlej, M. E. W. de Oliveira, M. Benchimol, M. L. Costa, C. Mermelstein, 2D and 3D-organized cardiac cells shows differences in cellular morphology, adhesion junctions, presence of myofibrils and protein expression. *PLOS ONE* **7**, e38147 (2012).
17. M. Noorman, M. A. G. van der Heyden, T. A. B. van Veen, M. G. P. J. Cox, R. N. W. Hauer, J. M. T. de Bakker, H. V. M. van Rijen, Cardiac cell–cell junctions in health and disease: Electrical versus mechanical coupling. *J. Mol. Cell. Cardiol.* **47**, 23–31 (2009).
18. H. Naito, I. Melnychenko, M. Didié, K. Schneiderbanger, P. Schubert, S. Rosenkranz, T. Eschenhagen, W. H. Zimmermann, Optimizing engineered heart tissue for therapeutic applications as surrogate heart muscle. *Circulation* **114**, I72–I78 (2006).
19. T. Boudou, W. R. Legant, A. Mu, M. A. Borochin, N. Thavandiran, M. Radisic, P. W. Zandstra, J. A. Epstein, K. B. Margulies, C. S. Chen, A microfabricated platform to measure and manipulate the mechanics of engineered cardiac microtissues. *Tissue Eng. Part A* **18**, 910–919 (2012).
20. N. Thavandiran, N. Dubois, A. Mikryukov, S. Massé, B. Beca, C. A. Simmons, V. S. Deshpande, J. P. McGarry, C. S. Chen, K. Nanthakumar, G. M. Keller, M. Radisic, P. W. Zandstra, Design and formulation of functional pluripotent stem cell-derived cardiac microtissues. *Proc. Natl. Acad. Sci. U.S.A.* **110**, E4698–E4707 (2013).
21. I. Y. Shadrin, B. W. Allen, Y. Qian, C. P. Jackman, A. L. Carlson, M. E. Juhas, N. Bursac, Cardiopatch platform enables maturation and scale-up of human pluripotent stem cell-derived engineered heart tissues. *Nat. Commun.* **8**, 1825 (2017).
22. D. Zhang, I. Y. Shadrin, J. Lam, H. Q. Xian, H. R. Snodgrass, N. Bursac, Tissue-engineered cardiac patch for advanced functional maturation of human ESC-derived cardiomyocytes. *Biomaterials* **34**, 5813–5820 (2013).
23. W. Bian, C. P. Jackman, N. Bursac, Controlling the structural and functional anisotropy of engineered cardiac tissues. *Biofabrication* **6**, 024109 (2014).
24. B. Liau, N. Christoforou, K. W. Leong, N. Bursac, Pluripotent stem cell-derived cardiac tissue patch with advanced structure and function. *Biomaterials* **32**, 9180–9187 (2011).
25. C. E. Rupert, K. L. K. Coulombe, IGF1 and NRG1 enhance proliferation, metabolic maturity, and the force-frequency response in hESC-derived engineered cardiac tissues. *Stem Cells Int.* **2017**, 7648409 (2017).
26. R. A. Li, W. Keung, T. J. Cashman, P. C. Backeris, B. V. Johnson, E. S. Bardot, A. O. T. Wong, P. K. W. Chan, C. W. Y. Chan, K. D. Costa, Bioengineering an electro-mechanically functional miniature ventricular heart chamber from human pluripotent stem cells. *Biomaterials* **163**, 116–127 (2018).
27. M. E. Kupfer, W.-H. Lin, V. Ravikumar, K. Qiu, L. Wang, L. Gao, D. Bhuiyan, M. Lenz, J. Ai, R. R. Mahutga, D. Townsend, J. Zhang, M. C. McAlpine, E. G. Tolkacheva, B. M. Ogle, In situ expansion, differentiation and electromechanical coupling of human cardiac muscle in a 3D bioprinted, chambered organoid. *Circ. Res.* **127**, 207–224 (2020).
28. K. Ronaldson-Bouchard, S. P. Ma, K. Yeager, T. Chen, L. J. Song, D. Sirabella, K. Morikawa, D. Teles, M. Yazawa, G. Vunjak-Novakovic, Advanced maturation of human cardiac tissue grown from pluripotent stem cells. *Nature* **556**, 239–243 (2018).
29. J. T. Hinson, A. Chopra, N. Nafissi, W. J. Polacheck, C. C. Benson, S. Swist, J. Gorham, L. Yang, S. Schafer, C. C. Sheng, A. Haghighi, J. Homsy, N. Hubner, G. Church, S. A. Cook, W. A. Linke, C. S. Chen, J. G. Seidman, C. E. Seidman, Titin mutations in iPS cells define sarcomere insufficiency as a cause of dilated cardiomyopathy. *Science* **349**, 982–986 (2015).
30. A. Leonard, A. Bertero, J. D. Powers, K. M. Beussman, S. Bhandari, M. Regnier, C. E. Murry, N. J. Sniadecki, Afterload promotes maturation of human induced pluripotent stem cell derived cardiomyocytes in engineered heart tissues. *J. Mol. Cell. Cardiol.* **118**, 147–158 (2018).
31. Z. Ma, N. Huebsch, S. Koo, M. A. Mandegar, B. Siemons, S. Boggess, B. R. Conklin, C. P. Grigoropoulos, K. E. Healy, Contractile deficits in engineered cardiac microtissues as a result of MYBPC3 deficiency and mechanical overload. *Nat. Biomed. Eng.* **2**, 955–967 (2018).
32. F. Weinberger, I. Mannhardt, T. Eschenhagen, Engineering cardiac muscle tissue: A maturating field of research. *Circ. Res.* **120**, 1487–1500 (2017).
33. W. L. Stoppel, D. L. Kaplan, L. D. Black, Electrical and mechanical stimulation of cardiac cells and tissue constructs. *Adv. Drug Deliv. Rev.* **96**, 135–155 (2016).
34. J. L. Ruan, N. L. Tulloch, M. V. Razumova, M. Saiget, V. Muskheli, L. Pabon, H. Reinecke, M. Regnier, C. E. Murry, Mechanical stress conditioning and electrical stimulation promote contractility and force maturation of induced pluripotent stem cell-derived human cardiac tissue. *Circulation* **134**, 1557–1567 (2016).
35. I. C. Turnbull, I. Karakikes, G. W. Serrao, P. Backeris, J.-J. Lee, C. Xie, G. Senyei, R. E. Gordon, R. A. Li, F. G. Akar, R. J. Hajjar, J.-S. Hulot, K. D. Costa, Advancing functional engineered cardiac tissues toward a preclinical model of human myocardium. *FASEB J.* **28**, 644–654 (2014).
36. I. Mannhardt, K. Breckwoldt, D. Letuffe-Brenière, S. Schaaf, H. Schulz, C. Neuber, A. Benzin, T. Werner, A. Eder, T. Schulze, B. Klampe, T. Christ, M. N. Hirt, N. Huebner, A. Moretti,

T. Eschenhagen, A. Hansen, Human engineered heart tissue: Analysis of contractile force. *Stem Cell Rep.* **7**, 29–42 (2016).

37. T.-Y. Lu, B. Lin, J. Kim, M. Sullivan, K. Tobita, G. Salama, L. Yang, Repopulation of decellularized mouse heart with human induced pluripotent stem cell-derived cardiovascular progenitor cells. *Nat. Commun.* **4**, 2307 (2013).
38. R. F. Wiegerinck, A. Cojoc, C. M. Zeidenweber, G. Ding, M. Shen, W. Joyner, J. D. Fernandez, K. R. Kanter, P. M. Kirshbom, B. E. Kogon, B. Wagner, Force Frequency relationship of the human ventricle increases during early postnatal development. *Pediatr. Res.* **65**, 414–419 (2009).
39. A. F. G. Godier-Furnémont, M. Tiburcy, E. Wagner, M. Dewenter, S. Lämmle, A. El-Armouche, S. E. Lehnart, G. Vunjak-Novakovic, W. H. Zimmermann, Physiologic force-frequency response in engineered heart muscle by electromechanical stimulation. *Biomaterials* **60**, 82–91 (2015).
40. Q. Jallerat, A. W. Feinberg, Extracellular matrix structure and composition in the early four-chambered embryonic heart. *Cell* **9**, 285 (2020).
41. L. D. Black, J. D. Meyers, J. S. Weinbaum, Y. A. Shvelidze, R. T. Tranquillo, Cell-induced alignment augments twitch force in fibrin gel-based engineered myocardium via gap junction modification. *Tissue Eng. Part A* **15**, 3099–3108 (2009).
42. S. D. Lundy, W.-Z. Zhu, M. Regnier, M. A. Laflamme, Structural and functional maturation of cardiomyocytes derived from human pluripotent stem cells. *Stem Cells Dev.* **22**, 1991–2002 (2013).
43. A. J. Price, A.-L. Cost, H. Ungewiß, J. Waschke, A. R. Dunn, C. Grashoff, Mechanical loading of desmosomes depends on the magnitude and orientation of external stress. *Nat. Commun.* **9**, 5284 (2018).
44. A. Blazeski, G. M. Kostecki, L. Tung, Engineered heart slices for electrophysiological and contractile studies. *Biomaterials* **55**, 119–128 (2015).
45. N. Bursac, K. K. Parker, S. Iravanian, L. Tung, Cardiomyocyte cultures with controlled macroscopic anisotropy: A model for functional electrophysiological studies of cardiac muscle. *Circ. Res.* **91**, e45–e54 (2002).
46. D.-H. Kim, E. A. Lipke, P. Kim, R. Cheong, S. Thompson, M. Delannoy, K.-Y. Suh, L. Tung, A. Levchenko, Nanoscale cues regulate the structure and function of macroscopic cardiac tissue constructs. *Proc. Natl. Acad. Sci. U.S.A.* **107**, 565–570 (2010).
47. A. Horváth, M. D. Lemoine, A. Löser, I. Mannhardt, F. Flenner, A. U. Uzun, C. Neuber, K. Breckwoldt, A. Hansen, E. Girdauskas, H. Reichenspurner, S. Willems, N. Jost, E. Wettwer, T. Eschenhagen, T. Christ, Low resting membrane potential and low inward rectifier potassium currents are not inherent features of hiPSC-derived cardiomyocytes. *Stem Cell Rep.* **10**, 822–833 (2018).
48. L. F. Santana, E. P. Cheng, W. J. Lederer, How does the shape of the cardiac action potential control calcium signaling and contraction in the heart? *J. Mol. Cell. Cardiol.* **49**, 901–903 (2010).
49. S. S. Nunes, J. W. Miklas, J. Liu, R. Aschar-Sobbi, Y. Xiao, B. Zhang, J. Jiang, S. Massé, M. Gagliardi, A. Hsieh, N. Thavandiran, M. A. Laflamme, K. Nanthakumar, G. J. Gross, P. H. Backx, G. Keller, M. Radisic, Biowire: A platform for maturation of human pluripotent stem cell–derived cardiomyocytes. *Nat. Methods* **10**, 781–787 (2013).
50. W. P. te Rijdt, Z. J. van der Klooster, E. T. Hoorntje, J. D. H. Jongbloed, P. A. van der Zwaag, F. W. Asselbergs, D. Dooijes, R. A. de Boer, J. P. van Tintelen, M. P. van den Berg, A. Vink, A. J. H. Suurmeijer, Phospholamban immunostaining is a highly sensitive and specific method for diagnosing phospholamban p.Arg14del cardiomyopathy. *Cardiovasc. Pathol.* **30**, 23–26 (2017).
51. K. Ronaldson-Bouchard, K. Yeager, D. Teles, T. Chen, S. Ma, L. J. Song, K. Morikawa, H. M. Wobma, A. Vasciaveo, E. C. Ruiz, M. Yazawa, G. Vunjak-Novakovic, Engineering of human cardiac muscle electromechanically matured to an adult-like phenotype. *Nat. Protoc.* **14**, 2781–2817 (2019).
52. K. Ye Morgan, L. D. Black III, It's all in the timing: Modeling isovolumic contraction through development and disease with a dynamic dual electromechanical bioreactor system. *Organogenesis* **10**, 317–322 (2014).
53. K. Y. Morgan, L. D. Black III, Mimicking isovolumic contraction with combined electromechanical stimulation improves the development of engineered cardiac constructs. *Tissue Eng. Part A* **20**, 1654–1667 (2014).
54. E. Rizzuto, S. Carosio, M. Faraldi, S. Pisu, A. Musarò, Z. Del Prete, A DIC based technique to measure the contraction of a skeletal muscle engineered tissue. *Appl. Bionics Biomech.* **2016**, 7465095 (2016).
55. K. J. Hansen, M. A. Laflamme, G. R. Gaudette, Development of a contractile cardiac fiber from pluripotent stem cell derived cardiomyocytes. *Front. Cardiovasc. Med.* **5**, 52 (2018).
56. R. E. Hershberger, D. J. Hedges, A. Morales, Dilated cardiomyopathy: The complexity of a diverse genetic architecture. *Nat. Rev. Cardiol.* **10**, 531–547 (2013).
57. N. N. Chattergoon, G. D. Giraud, S. Louey, P. Stork, A. L. Fowden, K. L. Thornburg, Thyroid hormone drives fetal cardiomyocyte maturation. *FASEB J.* **26**, 397–408 (2012).
58. O. Iglesias-García, S. Baumgartner, L. Macrí-Pellizzeri, J. R. Rodriguez-Madoz, G. Abizanda, E. Guruceaga, E. Albiasu, D. Corbacho, C. Benavides-Vallve, M. Soriano-Navarro, S. González-Granero, J. J. Gavira, B. Krausgrill, M. Rodriguez-Mañero, J. M. García-Verdugo, C. Ortiz-de-Solorzano, M. Halbach, J. Hescheler, B. Pelacho, F. Prósper, Neuregulin-1β induces mature ventricular cardiac differentiation from induced pluripotent stem cells contributing to cardiac tissue repair. *Stem Cells Dev.* **24**, 484–496 (2015).
59. S. S. Parikh, D. J. Blackwell, N. Gomez-Hurtado, M. Frisk, L. Wang, K. Kim, C. P. Dahl, A. Fiane, T. Tønnessen, D. O. Kryshtal, W. E. Louch, B. C. Knollmann, Thyroid and glucocorticoid hormones promote functional T-tubule development in human-induced pluripotent stem cell-derived cardiomyocytes. *Circ. Res.* **121**, 1323–1330 (2017).
60. D. V. Cokkinos, C. Belogianneas, Left ventricular remodelling: A problem in search of solutions. *Eur. Cardiol. Rev.* **11**, 29–35 (2016).
61. J. G. Seidman, C. Seidman, The genetic basis for cardiomyopathy. *Cell* **104**, 557–567 (2001).
62. E. D. Carruth, W. Young, D. Beer, C. A. James, H. Calkins, L. Jing, S. Raghunath, D. N. Hartzel, J. B. Leader, H. L. Kirchner, D. T. Smelser, D. J. Carey, M. A. Kelly, A. C. Sturm, A. Alsaid, B. K. Fornwalt, C. M. Haggerty, Prevalence and electronic health record-based phenotype of loss-of-function genetic variants in arrhythmogenic right ventricular cardiomyopathy-associated genes. *Circ. Genomic Precis. Med.* **12**, e002579 (2019).
63. R. Walsh, K. L. Thomson, J. S. Ware, B. H. Funke, J. Woodley, K. J. McGuire, F. Mazzarotto, E. Blair, A. Seller, J. C. Taylor, E. V. Minikel; Exome Aggregation Consortium, D. G. MacArthur, M. Farrall, S. A. Cook, H. Watkins, Reassessment of Mendelian gene pathogenicity using 7,855 cardiomyopathy cases and 60,706 reference samples. *Genet. Med.* **19**, 192–203 (2017).
64. J. S. Burchfield, M. Xie, J. A. Hill, Pathological ventricular remodeling: Mechanisms: Part 1 of 2. *Circulation* **128**, 388–400 (2013).
65. A. P. Voorhees, H.-C. Han, Biomechanics of cardiac function. *Compr. Physiol.* **5**, 1623–1644 (2015).
66. A. Lee, A. R. Hudson, D. J. Shiwarski, J. W. Tashman, T. J. Hinton, S. Yerneni, J. M. Bliley, P. G. Campbell, A. W. Feinberg, 3D bioprinting of collagen to rebuild components of the human heart. *Science* **365**, 482–487 (2019).
67. L. A. Macqueen, S. P. Sheehy, C. O. Chantre, J. F. Zimmerman, F. S. Pasqualini, X. Liu, J. A. Goss, P. H. Campbell, G. M. Gonzalez, S. J. Park, A. K. Capulli, J. P. Ferrier, T. Fettah Kosar, L. Mahadevan, W. T. Pu, K. K. Parker, A tissue-engineered scale model of the heart ventricle. *Nat. Biomed. Eng.* **2**, 930–941 (2018).
68. W. Keung, P. K. W. Chan, P. C. Backeris, E. K. Lee, N. Wong, A. O. T. Wong, G. K. Y. Wong, C. W. Y. Chan, B. Fermini, K. D. Costa, R. A. Li, Human cardiac ventricular-like organoid chambers and tissue strips from pluripotent stem cells as a two-tiered assay for inotropic responses. *Clin. Pharmacol. Ther.* **106**, 402–414 (2019).
69. E. McNally, M. Allikian, M. T. Wheeler, J. M. Mislow, A. Heydemann, Cytoskeletal defects in cardiomyopathy. *J. Mol. Cell. Cardiol.* **35**, 231–241 (2003).
70. M. Kawatou, H. Masumoto, H. Fukushima, G. Morinaga, R. Sakata, T. Ashihara, J. K. Yamashita, Modelling torsade de pointes arrhythmias in vitro in 3D human iPS cell-engineered heart tissue. *Nat. Commun.* **8**, 1078 (2017).
71. E. Sommariva, S. Brambilla, C. Carbucicchio, E. Gambini, V. Meraviglia, A. Dello Russo, F. M. Farina, M. Casella, V. Catto, G. Pontone, M. Chiesa, I. Stadiotti, E. Cogliati, A. Paolin, N. Ouali Alami, C. Preziuso, G. D'Amati, G. I. Colombo, A. Rossini, M. C. Capogrossi, C. Tondo, G. Pompilio, Cardiac mesenchymal stromal cells are a source of adipocytes in arrhythmogenic cardiomyopathy. *Eur. Heart J.* **57**, 1835–1846 (2016).
72. O. Caspi, I. Huber, A. Gepstein, G. Arbel, L. Maizels, M. Boulos, L. Gepstein, Modeling of arrhythmogenic right ventricular cardiomyopathy with human induced pluripotent stem cells. *Circ. Cardiovasc. Genet.* **6**, 557–568 (2013).
73. C. Kim, J. Wong, J. Wen, S. Wang, C. Wang, S. Spiering, N. G. Kan, S. Forcales, P. L. Puri, T. C. Leone, J. E. Marine, H. Calkins, D. P. Kelly, D. P. Judge, H.-S. V. Chen, Studying arrhythmogenic right ventricular dysplasia with patient-specific iPSCs. *Nature* **494**, 105–110 (2013).
74. A. Asimaki, A. G. Kleber, J. E. Saffitz, Pathogenesis of arrhythmogenic cardiomyopathy. *Can. J. Cardiol.* **31**, 131–1324 (2015).
75. J. Gomes, M. Finlay, A. K. Ahmed, E. J. Ciaccio, A. Asimaki, J. E. Saffitz, G. Quarta, M. Nobles, P. Syrris, S. Chaubey, W. J. McKenna, A. Tinker, P. D. Lambiase, Electrophysiological abnormalities precede overt structural changes in arrhythmogenic right ventricular cardiomyopathy due to mutations in desmoplakin-A combined murine and human study. *Eur. Heart J.* **33**, 1942–1953 (2012).
76. X. Lian, J. Zhang, S. M. Azarin, K. Zhu, L. B. Hazeltine, X. Bao, C. Hsiao, T. J. Kamp, S. P. Palecek, Directed cardiomyocyte differentiation from human pluripotent stem cells by modulating Wnt/β-catenin signaling under fully defined conditions. *Nat. Protoc.* **8**, 162–175 (2013).
77. S. Tohyama, F. Hattori, M. Sano, T. Hishiki, Y. Nagahata, T. Matsuura, H. Hashimoto, T. Suzuki, H. Yamashita, Y. Satoh, T. Egashira, T. Seki, N. Muraoka, H. Yamakawa, Y. Ohgino, T. Tanaka, M. Yoichi, S. Yuasa, M. Murata, M. Suematsu, K. Fukuda, Distinct metabolic flow enables large-scale purification of mouse and human pluripotent stem cell-derived cardiomyocytes. *Cell Stem Cell* **12**, 127–137 (2013).

78. K. Okita, Y. Matsumura, Y. Sato, A. Okada, A. Morizane, S. Okamoto, H. Hong, M. Nakagawa, K. Tanabe, K. I. Tezuka, T. Shibata, T. Kunisada, M. Takahashi, J. Takahashi, H. Saji, S. Yamanaka, A more efficient method to generate integration-free human iPS cells. *Nat. Methods* **8**, 409–412 (2011).
79. K. Takahashi, K. Tanabe, M. Ohnuki, M. Narita, T. Ichisaka, K. Tomoda, S. Yamanaka, Induction of pluripotent stem cells from adult human fibroblasts by defined factors. *Cell* **131**, 861–872 (2007).
80. P. W. Burridge, A. Holmström, J. C. Wu, Chemically defined culture and cardiomyocyte differentiation of human pluripotent stem cells. *Curr. Protoc. Hum. Genet.* **87**, 21.3.1–21.3.15 (2015).
81. L. Martin, A. Grigoryan, D. Wang, J. Wang, L. Breda, S. Rivella, T. Cardozo, L. B. Gardner, Identification and characterization of small molecules that inhibit nonsense-mediated rna decay and suppress nonsense p53 mutations. *Cancer Res.* **74**, 3104–3113 (2014).
82. Y. Sun, Q. Jallerat, J. M. Szymanski, A. W. Feinberg, Conformal nanopatterning of extracellular matrix proteins onto topographically complex surfaces. *Nat. Methods* **12**, 134–136 (2015).

Acknowledgments: Part of the work was performed at the UMCG Imaging and Microscopy Center (UMIC), for which we express our gratitude. **Funding:** This work was supported by the Human Frontier Science Program (grant number RGY 0071/2014 to P.v.d.M. and A.W.F.), the NIH (grant number DP2HL117750 to A.W.F.), the Office of Naval Research (grant number N00014-17-1-2566 to A.W.F.), Additional Ventures Cures Collaborative (to A.W.F.), and the Dowd Fellowship and Presidential Fellowship, Carnegie Mellon University (to J.M.B.) and in part by the European Research Council (grant number: ERC-2016-StG – 715732 to P.v.d.M.).

Author contributions: Design study: A.W.F., P.v.d.M., J.M.B., and M.C.S.C.V. Establishing methods: J.M.B., M.C.S.C.V., M.F.H., R.M.D., I.B., D.J.S., J.W.T., B.C., and M.C.B. Conducting experiments: J.M.B., M.C.S.C.V., R.M.D., A.K., A.L., Y.S., and R.N.P. Data processing: J.M.B., M.C.S.C.V., D.K., and I.B. Data collection: J.M.B., M.C.S.C.V., and R.N.P. Figure contributions: J.M.B., M.C.S.C.V., L.V., A.S.T., I.B., D.J.S., J.W.T., R.N.P., D.A.P., A.J.H.S., and J.D.H.J. Critical data interpretation: All. **Competing interests:** Carnegie Mellon University has filed for patent protection on the technology described here, and J.M.B., R.M.D., and A.W.F. are named as inventors on the patent [PCT/US2018/000165 (2018-017) – Three Dimensional Microtissues with Integrated Mechanical Loading]. The other authors declare no competing interests. **Data and materials availability:** All data associated with this study are present in the paper or the Supplementary Materials.

Submitted 5 June 2020
Accepted 2 July 2021
Published 21 July 2021
10.1126/scitranslmed.abd1817

Citation: J. M. Bliley, M. C. S. C. Vermeer, R. M. Duffy, I. Batalov, D. Kramer, J. W. Tashman, D. J. Shiwarski, A. Lee, A. S. Teplenin, L. Volkers, B. Coffin, M. F. Hoes, A. Kalmykov, R. N. Palchesko, Y. Sun, J. D. H. Jongbloed, N. Bomer, R. A. de Boer, A. J. H. Suurmeijer, D. A. Pijnappels, M. C. Bolling, P. van der Meer, A. W. Feinberg, Dynamic loading of human engineered heart tissue enhances contractile function and drives a desmosome-linked disease phenotype. *Sci. Transl. Med.* **13**, eabd1817 (2021).